UC Irvine

UC Irvine Electronic Theses and Dissertations

Title

Characterizing breast cancer invasive potential using combined label-free multiphoton metabolic imaging of cellular lipids and redox state

Permalink

https://escholarship.org/uc/item/4717g784

Author

Hou, Jue

Publication Date

2017

Copyright Information

Peer reviewed|Thesis/dissertation

UNIVERSITY OF CALIFORNIA,
IRVINE

Characterizing breast cancer invasive potential using combined label-free multiphoton

metabolic imaging of cellular lipids and redox state

DISSERTATION

submitted in partial satisfaction of the requirements
for the degree of

DOCTOR OF PHILOSOPHY

in Biomedical Engineering

by

Jue Hou

Dissertation Committee:
Professor Bruce J. Tromberg, Chair
Associate Professor Eric O. Potma
Associate Professor Elliot Botvinick

2017

TABLE OF CONTENTS

LIST OF FIGUREs

LIST OF TABLES

ACKNOWLEDGEMENTS

I acknowledge I have reprint permission from the publishers of my work to incorporate that work in my dissertation. In particular, I acknowledge permission from SPIE. Individual contributions are pertinently cited.

I'd like to further thank the support, guidance, and encouragement of my advisers Prof. Bruce J. Tromberg and Prof. Eric O. Potma, and of my committee member Prof. Elliot Botvinick. It is from them that I learned how to be a researcher and a decent man. I wish to extend my gratitude to all the members in Beckman Laser Institute. From Mihaela and Tatiana, for welcoming me into the lab and guiding my first research steps and I really appreciate all the helps they offered to me both on scientific researches and my personal life. I would also like to thank all the members works in the BLI front desks especially Jan, Hanna, Allen and Linda. I also appreciate the insights brought by the visiting scientists in the lab during the past 5 years. I want to acknowledge the biomedical engineering department staff members as well, they are always helpful and diligent.

I would like to kindly express my gratitude to all my collaborators from Razoenova Lab, especially Heather Wright for all her hard work. Also, deep gratitude to the Edinger Lab. Prof. Aimee Edinger and Dr. Seong Kim.

Finally, I want to deeply thank my family and friends for their support. I really appreciate the accompany with Jie and Angie and the fun they brought to my life.

CURRICULUM VITAE

Jue Hou

EDUCATION

2011 - 2017   Biomedical Engineering in University of California, Irvine.

Supervisor: Bruce Tromberg and Eric Potman. GPA 3.94

2007 - 2011   The Department of Optoelectronics in Huazhong University of Science and Technology.

Supervisor: Deming Liu.

RESEARCH EXPERIENCE

2011 - 2017   Graduate Research Assistant in Biomedical Engineering, University of California, Irvine.

The correlation of breast cancer cell metabolism and cancer metastatic potential with nonlinear optical microscope.

2007 - 2011   Research Intern in Wuhan National Laboratory for Optoelectronics.

Real-time Imaging for FD-OCT Systems Based on the Mixing Computer Programming of Labview and Graphic Processing Unit programming

2010 (summer)   Research Intern in Photonics and Optoelectronicc Laboratory, Johns Hopkins.

The application of interferometric synthetic aperture microscopy (ISAM) in the post-processing of an OCT system

2009 (summer)   Yangtze Optical Fibre and Cable Company Ltd., Wuhan, China

The best fusion parameters between PCF and SMF.

PUBLICATIONS

1) Hou J*, Wright HJ*, Chan N, and et al.. Correlating two-photon excited fluorescence imaging of breast cancer cellular redox state with seahorse flux analysis of normalized cellular oxygen consumption. J Biomed Opt, 26(1), 2016.

2) Kim SM, Roy SG, Chen B, and et al.. Targeting cancer metabolism by simultaneously disrupting parallel. J Clin Invest, 126(11), 2016.

3) Balu M, Mikami H, Hou J and et al.. Rapid mesoscale multiphoton microscopy of human skin. Biomed. Opt. Express, 7(11), 2016.

4) Balu M*, Saytashev I*, Hou J, and et al.. Sub-40 fs, 1060-nm Yb-fiber laser enhances penetration depth in nonlinear optical microscopy of human skin. J Biomed Opt, 20(12), 2015.

5) Qing Xiao, Jue Hou, and Ling Fu. Real Time Display with Large Field of View on Fourier Domain Optical Coherence Tomography at 1310 nm Wavelength for Dermatology. Laser Physics, 22(6), 2012.

ORAL and POSTER PRESENTATIONS

1) SPIE Photonic West, 2015. Oral presentation. Optical Imaging of Breast Cancer Metabolic Signatures in 3D Acini Utilizing Nonlinear Optical Imaging.

2) Biomedical Optical Congress, 2016. Oral presentation. Two-Photon Excited Fluorescence Imaging and Oxygen Flux Analysis of Optical Redox Ratios in Breast Cancer Cells.

3) SPIE Photonic West, 2017. Poster presentation. Combined glucose and lipid metabolism reveals the correlation of cancer metabolism and invasiveness.

ABSTRACT OF THE DISSERTATION

Characterizing breast cancer invasive potential using combined label-free multiphoton metabolic imaging of cellular lipids and redox state

By

Jue Hou

Doctor of Philosophy in Biomedical Engineering

University of California, Irvine, 2017

Professor Bruce J. Tromberg, Chair

Aerobic glycolysis (Warburg effect) is accompanied by significant alterations in cellular redox state and constitutes one of the hallmarks of cancer cell metabolism. Label-free multi-photon microscopy (MPM) methods based on two-photon excited fluorescence (TPEF) have been used extensively to form high-resolution images of redox state in cells and tissues based on intrinsic NADH and FAD+ fluorescence. However, changes in cellular redox alone are insufficient to fully characterize cancer metabolism and predict invasive potential. We demonstrate that label-free MPM measurements of TPEF-derived redox state (optical redox ratio, ORR = FAD+/(FAD + NADH)) combined with coherent Raman imaging of lipid formation can be used to quantitatively characterize cancer cells and their relative invasive potential. In addition, we confirm, using coherent Raman and deuterium labeling methods, that glucose is a significant source for the cellular synthesis of lipid biomass in glycolytic breast cancer cells. Live cell metabolism was imaged in 3D models of primary mammary epithelial cells (PME) and 2 cancer cell lines, T47D and MDA-MB-231. While we

observed overlap in the distribution of the optical redox ratio between these different cell lines, the combination of ORR and lipid volume fraction derived from coherent Raman signals provided complementary independent measures and clear separation. Furthermore, we observed an increase in both lipid synthesis and consumption rates in E2-treated T47D cancer cells cultured in deuterated glucose by tracking the formation and disappearance of deuterated lipids. These results suggest that due to the relatively wide range of ORR values that reflect the natural diversity of breast cancer cellular redox states, the addition of lipid signatures obtained from coherent Raman imaging can improve our ability to characterize and understand key metabolic features that are hallmarks of the disease.

Chapter 1

Cancer Metabolism

"One general law, leading to the advancement of all organic beings, namely, multiply, vary, let the strongest live and the weakest die."

— Charles Darwin, The Origin of Species

1.1 Glucose – the key player of cell metabolism

1.1.1 Fuel the energy production

All the human behaviors, including growth, muscle contraction and reproduction, requires energy. Therefore, we must have a constant intake of food to maintain the biological order and keep us alive. The nutrients can come in different forms, however, glucose is particularly important. It is the major source of energy for all the cells in human body and supplies almost all for the neurons, fibroblasts and blood cells [1-3]. Moreover, alterations of glucose kinetics can be correlated with critical illness [4]. Thus, the delivering of glucose molecules to each individual cell are crucial and are constantly done by our digestive and cardiovascular systems throughout our life. Within each cell, the chemical bonds of glucose are continuously broken down to produce the energy and the rate is strongly related with cell functions. Unlike burning, the cells release the energy

in the glucose through a series of reactions and store them in the adenosine triphosphate (ATP) molecules which are used to fuel other processes. The main pathways of glucose catabolism are known to be glycolysis and oxidative phosphorylation (OxPhos) which have been studied and fully established for more than 100 years [5].
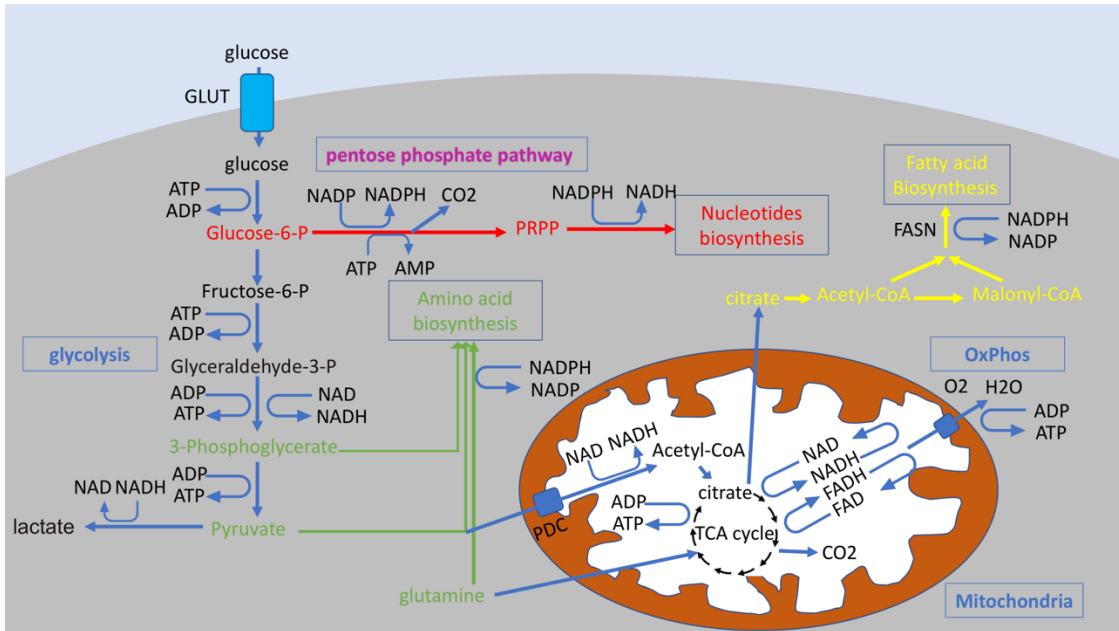
Figure 1.1. Metabolic pathways of glycolysis, OxPhos and biosynthesis.

The study of glycolysis was first started in the 19th century inspired by wine industry. It was found that the yeasts have a reduced glucose consumption rate in aerobic conditions and inappropriate control of the oxygen level would turn the wine distasteful [6]. From there, the entire glycolytic pathways, its regulation and integration of other metabolic pathways were understood piece by piece (figure 1.1). Glycolysis initiates from the phosphorylation of a glucose molecule which takes two ATPs as the seeding energy. The end-product is a fructose-1,6-biphosphate which is very unstable and can be degraded into two interconvertible three carbon molecules. Both triose sugars enter the pay-off phase and ultimately generate 2 pyruvates, 4 ATPs and 2 NADH in total. The

pyruvate is then fermented into ethanol and secreted by the yeast as a waste. The entire process does not require the existence of oxygen and happens in the cell cytosol. In human, the glucose is following a similar pathway but fermented into lactate acid instead of ethanol.

The finding of OxPhos greatly benefited from the studies on glycolysis, especially the investigation of the disappearance of lactate acid under aerobic condition. It was found that OxPhos initiated from glycolysis but the end-product was further oxidized into carbon dioxide and water instead of fermentation. The two processes are linked by pyruvate dehydrogenase complex on the membrane of an organelle called mitochondria. It transfers the two pyruvates, created by glycolysis, into mitochondria and convert them into acetyl coenzyme A (acetyl-CoA) and produce two molecules of CO_2 and NADH. The acetyl-CoA enter the tricarboxylic acid (TCA) cycle, also known as Krebs cycle, to be fully oxidized to 4 CO_2 molecules and reducing six NAD+ molecules to NADH. The TCA cycle also produces 2 $FADH_2$ and 2 ATPs. The final step comprises the secretion of protons in NADH and $FADH_2$ from the protein complex out of the inner membrane of mitochondria. It establishes a proton gradient across the inner membrane and create an electrochemical potential which is used by a protein complex to drive the phosphorylation of ADPs to produce ATPs. At the same time, the electrons are transferred to oxygen molecules on the electron transport chain to form water molecules. Compared to glycolysis, oxidative phosphorylation is 18 times more efficient in generating ATPs from one glucose molecule. However, this process only happens inside the mitochondrion in eukaryotic cells and requires the existence of oxygen.

1.1.2 Supply of biomass synthesis

To maintain homeostasis, a subpopulation of cells remains the capability of proliferation which requires more than just energy. As they divide, a constant supply of basic building blocks is needed which includes cell nucleotides (DNA/RNA), lipids (cell membrane) and amino acids (proteins). Although these nutrients can be acquired from the microenvironment, all the fast proliferating cells prefer *de novo* synthesis. The major donor of the carbon source is, again, glucose [7]!

Despite the large varieties of the sizes and functions of cells, all the cells in our body share the same genetic information encoded in DNA. To enable mitosis, the cells must provide ~6.5pg nucleotides for DNA replication [8]. The synthesis of most nucleotides requires the assembly of 9 to 10 carbon atoms. Half of the carbons come from 5-phosphoribosyl-α-pyrophosphate (PRPP) which can be derived from phosphorylated glucose at the beginning of glycolysis. The pathway that convert glucose to PRPP to enable to nucleotide synthesis is known as pentose phosphate pathway (PPP).

In addition to cell nucleus and RNA, human cells also have complex membrane system including plasm membrane, mitochondria, endoplasmic reticulum and Golgi apparatus. Whether the organelle has one layer or two layers of membrane, it all consists of a phospholipid bilayer embedded with glycolipid and cholesterol. Thus, the doubling of a cell has extensive demands of lipid content and the cells use glucose to generate lipid precursor – acetyl-CoA. Acetyl-CoA is produced at the beginning of oxidative phosphorylation inside mitochondria, however, it cannot be utilized for lipid biosynthesis which happens in cytosol. Instead, the acetyl-CoA enters the TCA cycle and be

metabolized into citrate which can be exported to cell cytosol and converted back to acetyl-CoA by ATP citrate lyase. With additional ATPs, the acetyl-CoA can be further metabolized into malonyl-CoA which acts together with acetyl-CoA for lipid synthesis which is catalyzed by fatty acid synthase (FASN).

Lastly, the requirement for protein, which takes up to 50% of dry cell mass, imposes the largest stress for proliferation cells. However, the fast up-taking glucose rate and precursors produced by the intermediates of glycolysis offers a solution. 3-phosphoglycerate and pyruvate act as carbon donors and can be directly used for synthesis of most nonessential amino acid. The synthesis of some other amino acids prefers a different source of carbon which relies more on the glutamine. The prostate cancer cells have demonstrated a specific glutamine dependence rather than glucose.

1.2   The famous Warburg effect

From the above, OxPhos is much more efficient in generating energy than glycolysis. It would be more beneficial for cancer cells to have enhanced OxPhos rate to meet the high demand of ATPs during cell proliferation and migration. However, it was observed that the cancer cells prefer glycolysis even in an oxygen rich environment. The aerobic glycolysis of cancer cells is well known as the famous Warburg effect and was first reported by Otto Warburg in 1926. In the paper, he wrote "It could be said of tumors, with their varying cancer cell content, that they ferment more strongly the more cancer cells they contain" [9].

At first glance, it was confusing. Why and how cancer cells reprogram to a less efficient pathway of energy production was elusive. Otto Warburg originally hypothesized that cancer cells have impaired mitochondria functions that leads to defect aerobic respiration. Hence, the production of ATPs fully relies on glycolysis. However, further studies demonstrated that isolated tumor mitochondria are as efficient as normal mitochondria for aerobic respiration. Now, more and more researchers believe that such metabolic adaptation is beneficial for fast cell proliferation, a notion supported by observations that 1) several mutations that affect cancer proliferation also regulate metabolic pathways [10, 11]; and 2) normal cells display higher rates of glycolysis when treated with growth factors to stimulate cell proliferation [7, 12, 13].

Let's take a closer look at fast proliferating cells. It is not hard to find that there are not only energy requirements but also functional needs during mitosis. The most prominent one is the doubling of the cell's biomass which includes amino acid, fatty acid and nucleotides. The biosynthetic flux of a palmitate molecule, for example, requires 7 ATPs, 16 carbons and 14 NADPH in total. For a single glucose molecule, it can be metabolized to generate 36 ATPs (OxPhos) or 30 ATPs and two NADPHs (pentose phosphate pathway, PPP) or 2 ATPs plus 6 carbons (glycolysis) (figure 1.2). With some simple calculations, we can tell that the demand for carbons and NADPH are the real bottleneck of the macromolecule biosynthesis rather than energy. From this perspective, even though fully catabolize the glucose molecule into CO_2 and H_2O is efficient in ATP production, it is a waste of carbons and reducing capabilities which are more crucial for cell proliferation. The fast dividing cells must reprogram in a way to meet the demand of carbon sources and reducing equivalents. Moreover, the glucose utilization rate of

glycolysis is 10-100 times faster than oxidative phosphorylation which enables

continuous uptake of nutrient. This metabolic reprogramming gives cancer cells clear

advantage over adjacent stromal cells when competing for limited glucose and nutrient in

their microenvironment. Thus, the switching from oxidative phosphorylation to

glycolysis is an adaptation to maximize the rapid uptake and incorporation of nutrients

for biosynthesis [14]
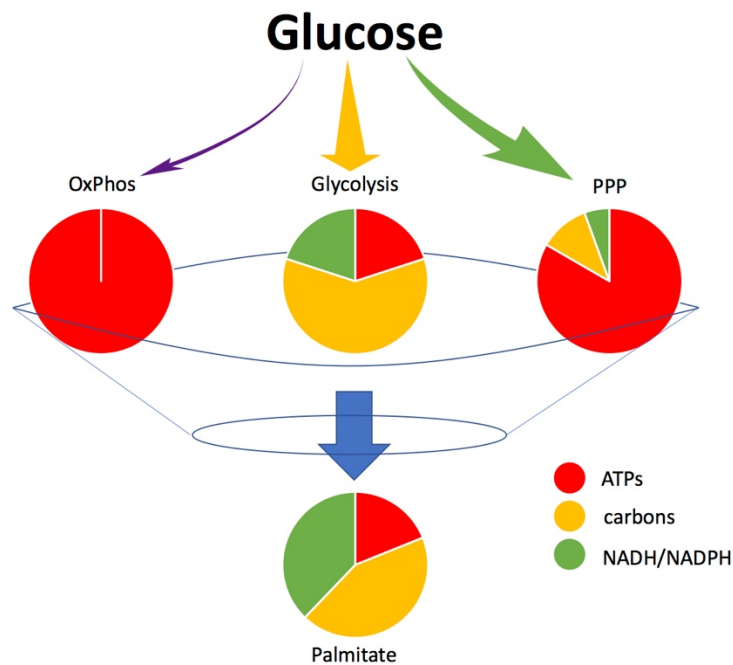
Figure 1.2. the biochemical demand for palmitate synthesis. The red parts represent the ATPs the process

can produce/utilize; the yellow parts represent the number of carbons the process can produce/utilize; and

the green parts represent the NAD(P)H the process can produce/utilize.

1.3   Cancer metabolism in biomedical application

1.3.1 Biomakers for cancer diagnosis

Currently, Warburg effect is considered an important biomarker for all types of cancers.

It is treated as one of the hottest topics in cancer society and the genetic origin of the

metabolic adaptation and its influence on cancer survival has been intensively studied. Not surprising, a lot of genes involved in cellular metabolism were found overexpressing in tumor cells and, thus, provided potential biomarkers for cancer detection.

Phosphatidyle inositol 3-kinases (PI3K) are a family of enzymes that regulate cellular functions including proliferation, differentiation and motility. The PI3Ks get phosphorylated in the cell membrane and can activate protein kinase B (also known as AKT) which has a number of downstream effects. Most importantly, the PI3K/AKT/mTOR pathway has been identified to be overexpressed in numerous tumor cells [15]. The activation of this cascade can increase the synthesis and translocation of glucose transporter (GLUT) to the plasma membrane and increase the glucose uptake rate. Moreover, the phosphatase and tensin homolog (PTEN), the PI3K inhibitor, is discovered to be lost in many tumor cells which further benefit the intensive demand for glucose. PGC-1a is another regulator for energy metabolism and was found to affect cancer invasiveness. and has been found to be correlated with different cancer invasiveness [16]. The PGC-1a increases the cancer metastatic potential by increasing oxidative phosphorylation, mitochondria biogenesis and oxygen consumption rate. 11 out of 13 lesions from patients who had confirmed lung metastases were reported PGC-1a positive.

Most normal cells prefer replenishing their fatty acid storage from circulating lipids. Except for liver, adipose tissue and hormone sensitive cells, fatty acid synthase (FASN) is normally inactive in differentiated cells. However, various tumor cells and lesions were observed favoring *de novo* lipid synthesis even in a well-nourished environment. Such cancer phenotype is associated with increased activities and overexpression of lipogenesis genes including FASN. Although both the normal and

cancer cells share identical intracellular signaling downstream pathways, the FASN expression in tumor cells seem to be insensitive to nutritional signals. The hyperactivity of FASN has been reported in in most of human epithelial cancers and neoplastic lesions and is correlated with higher recurrence rate and death rate [17, 18]. With constant high expression level of FASN, the cancer cells quickly use the intermediate products of glycolysis for fatty production in support of fast cell proliferation. Jin-xin et al reported increased cholesterol ester in prostate cancer cells.

The biochemical and molecular studies on the cancer cells brought us one step further closer to understand Warburg effect and provided scientific foundations to use it for cancer diagnosis. Currently, positron emission tomography, magnetic resonance imaging and mass spectrometry take advantage of isotope labelling and have already been used for cancer diagnosis based on their abnormal metabolism [19-21]. Magnetic resonance imaging, using time-resolved multiband radio-frequency excitation, revealed lactate accumulation in different stages of tumors as derived from hyperpolarized C^{13} labelled pyruvate [22]. Liquid chromatography-mass spectrometry and isotope labeling (C^{13} and N^{15}) has been used to observe the atomic contribution of acyl-coenzyme A from glucose, glutamine and propionate [23]. Due to the high glucose-based biosynthesis rate, the cancer cells also accumulate glucose analogue fluorodeoxyglucose (FDG) which is used contrast agen in PET scan [24]. All these observations further prove the potential of using metabolism for early and non-invasive cancer detection.

1.3.2 Personalized treatment

The current treatment regime for cancer is chemotherapy which is a combination of different drugs that target fast proliferating cells. Based on the doctor's experience, the recipe of cocktail can vary from patient to patient. However, about 30% of the patients will gain no benefit but still have to suffer from the side effects. Moreover, doctors receive little input until the completion of the treatment. Thus, there is a significant interest in identifying biomarkers that can predict drug response and provide oncologist dynamic feedbacks for better decision-making.

The cancer cells rely heavily on the aerobic glycolysis to support their fast proliferation rate. The chemotherapy that limit the cancer mitosis would affect their anabolic process at the very early stage. Such alterations of cell metabolism can be monitored and used as a predictor for cancer drug response [25-28]. Walsh *et al.* used optical imaging to dynamically monitor the metabolic changes of HER2+ breast cancer organoids in response to trastuzumab treatment. The authors observed an increase of free NADH in cancer cells that respond to chemotherapy as early as 48 hours [29]. Similar findings were found on mice xenograft where the cancer cells demonstrated early metabolic response form smaller tumor after 12 days. Albert Cerussi *et al.* used diffuse optical spectroscopic imaging modality to monitor the tumor metabolism before, in the middle and after completion of neoadjuvant chemotherapy on 36 patients noninvasively [30]. The oxy- and deoxyhaemoglobin, lipid and water in the tumor sites were found to be strongly correlated with pathological response. The combining of metabolic measurement with microplate reader can push forward personalized treatment and reduce the failure rate.

1.3.3 Novel target for cancer treatment

Cancer metabolism is a direct result of mutations of oncogenes and tumor-suppressor genes which facilitate cancer proliferation, malignant transformation and drug resistance. This reveals a possible "Achilles heel" which potentially works on all types of cancer and can be targeted precisely. Compromise or inhibit the key metabolic pathways would break the homeostasis and deprive cancer cells with metabolites that are essential for proliferation or migration.

Due to the importance of PI3K/AKT/mTOR pathway in cell proliferation and growth, it has been investigated for its therapeutic potential since its identification. A number of inhibitors has been evaluated in preclinical studies and some have been approved by US Food and Drug Administration. It can be categorized as PI3K inhibitor, PI3K-mTOR dual inhibitor and mTOR inhibitor. Rapamycin and its analogs (temsirolimus, everolimus and ridaforolimus) were among the very first drugs get approved by FDA. They can crosslink the FK506 protein through its methoxy group and form a complex which further bind to mTOR to inhibit its downstream signaling [31]. Rapalogs has demonstrated clear clinical benefits over breast cancer, melanoma, lymphoma, small-cell lung cancer and especially for renal cell carcinoma [32-35]. In a phase III trial, 209 patients who received 25mg temsirolimus intravenously every week demonstrated 49% increase of overall survival [36]. To achieve better therapeutic results, rapalogs have been administrated in combination with other chemotherapy drugs and were found to be synergetic with paclitaxel, carboplatin, cisplatin, vinorelbine, doxorubicin and campthotecin by promoting cancer cell apoptosis both *in vivo* and *in vitro* [37, 38]. Since then, more than 30 small molecules targeting PI3K entered clinical

trials. In 2014, Idellisb, which blocks the p110δ of PI3K, was approved for treatment of relapsed chronic lymphocytic leukemia, follicular B-cell non-Hodgkin lymphoma and relapsed mall lymphocytic lymphoma [39].

PTEN is noted to be one of the most frequently deleted or muted tumor suppressor gene in prostate, lung, breast and glioblastoma [40]. The loss of PTEN is commonly associated with poor drug response and increased cancer metastasis by increased activation of PI3K. Moreover, the reactivation of PTEN can activate FoxO transcriptional factor and induce cell apoptosis [41]. Knocking down the PTEN was observed with increased estrogen receptor transcriptional activity and increased resistance of ER positive breast cancer cells to tamoxifen and fulvestrant [42]. Hopkins *et al.* reported an engineered translational variant of PTEN which is membrane-permeable and can be secreted from cells [43]. The exogenous agent has been observed to induce tumor death both *in vitro* and *in vivo*. Seong et al. reported a synthetic sphingolipid (SH-BC-893) which triggers nutrient transporter internalization and starve the PTEN deficient cancer cells to death [44].

Elevated fatty acid biosynthesis is another hallmark for tumor. The high mitotic rate of cancer cells imposes a huge pressure on lipogenesis. To facilitate the production of cell membrane and organelles, the FASN is significantly upregulated in many cancer types but remains low expression level in normal tissues. Orlistat is FDA approved drug which was originally developed to treat obesity by preventing the hydration of triglyceride and make it unabsorbable by the GI track. In 2004, Kridel et al. found that orlistat can also inhibit FASN on its thioesterase domain and induce tumor cell apoptosis

in vitro [45]. However, its low cell permeability, low solubility and side-effects limit its usage in cancer treatment [46]. More recently, new synthetic FASN inhibitor (C93 or FAS93) was developed to treat lung cancer without anorexia or weight loss. The C93 was given orally with 100mg/(Kg*day) on mice bearing H460 and A549 cell lines derived lung cancer xenograft [47]. Significant tumor shrinkage was observed in both groups without noticeable weight loss or other toxicity.

Other metabolic related oncogenic mutations in cancer cells has also been targeted including sterol regulatory element-binding protein 1 (SREBP-1), pyruvate kinase M2 (PKM2), isocitrate dehydrogenase 1/2 (IDH), MYC, glucokinase (HK), mitogen-activated protein kinase (MAPK) and etc have also been intensively reviewed [48-51].

Chapter 2

Nonlinear Imaging Microscope

2.1 Two photon excited fluorescence and second harmonic generation

2.1.1 Imaging mechanism

TPEF microscopy SHG are two members of the big nonlinear optical imaging family in which two or more photons induce the electronic transition from ground state to excited state. As shown in figure 2.1, TPEF microscope requires two photons, each has half of the energy as one photon excitation, to arrive at the molecule at the same time. Thus, we can excite the fluorophores with longer wavelengths to minimize the scattering in tissue and increase the imaging depth. With Olympus XLUMPlanFl 20x 0.95NA and exogenous fluorescence dye, Kobat *et al.* were able to perform *in vivo* imaging on mouse cortex at a depth of 1.6 mm [52]. Other than the increased penetration depth, the utilization of near-infrared/infrared light reduces photodamage to live cells and tissue. Moreover, the fluorescence signal intensity is proportional to the square of excitation power and, therefore, only the fluorophores in the small focal volume can be excited.

Similarly, SHG also requires the absorption of two photons but the electrons are excited to a virtual state and drop to the ground state immediately with an emission of photon. The physics of SHG determines that the emission wavelength to be exactly half of the excitation photons and the process has extremely short lifetime. The SHG follows the same power rule as TPEF but only allowed in noncentrosymmetric media. Thus, the biological molecules that can generate SHG signal are very limited even though they do not need any extrinsic probes. SHG microscopy has been mostly used to image collagen structures and organizations in biological tissue which were proven to be important for cancer development and would healing [53-56].
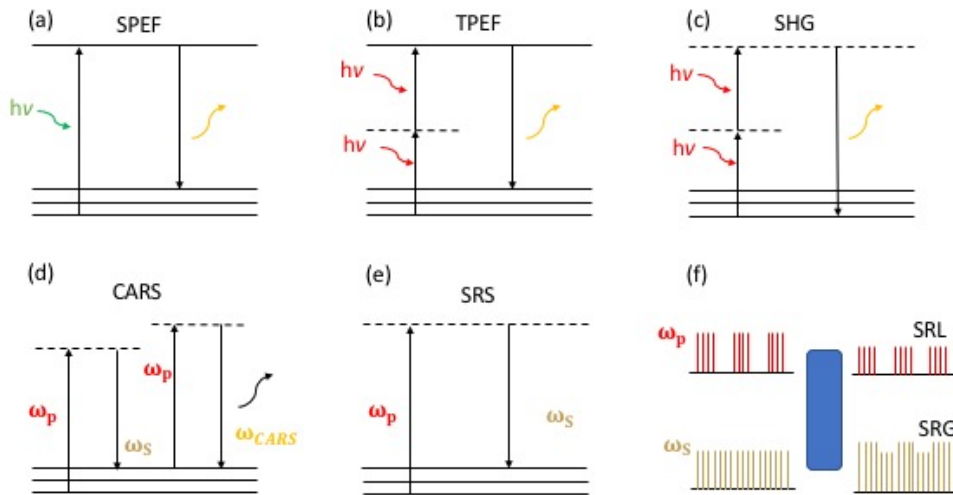
Figure 2.1. Illustration of different types of light matter interactions. (a) Single photon excited fluorescence (SPEF); (b) two photon excited fluorescence (TPEF); (c) second harmonic generation (SHG); (d) coherent anti-Stokes Raman scattering (CARS) and (e) stimulated Raman scattering (SRS). (f) the energy transfer from pump beam to Stokes beam in SRS microscope.

However, there is no free meal. The main impediment for implementing TPEF and SHG is the cost of the instrumentation which mainly comes from the laser source. Based on quantum mechanics, the chances (susceptibility) of TPEF and SHG are very small and, thus, requires high photon influx to generate detectable signal. To achieve that, the system need femtosecond laser source to efficiently generate the nonlinear signal.

2.1.2 Endogenous fluorophores

There are a lot of biomolecules that can emit light in the visible range when excited at proper wavelengths (table 2.1). The quantum yield and spectrum properties of these native fluorophores can be affected by the state of the microenvironment and, thus, provide functional and morphological information of the living system. Unlike conventional staining, the autofluorescence does not require complicated sample preparation and can ruled out the complexity induced by exogenous chemicals. When combined with optical imaging, tissue beneath the surface can be examined without disturbance and provide possibility for noninvasive optical biopsy [57].

molecule	excitation (nm)	emission (nm)
tryptophan	280	300-350
melanin	broad	360-560
retinol	330	500
Flavins	380-490	520-560
NADH	340	400-550
elastin	370	420-510
collagen	330	305-450

Table 2.1. The excitation and emission wavelengths of endogenous fluorophores.

Among the endogenous fluorophores, several have been investigated for their potential in cancer diagnosis. Increased tryptophan level has been observed to be correlated with cancer risks by inhibiting interleukin-10 secretion in breast, lung and brain tumors [58, 59]. Sordillo LA *et al.* observed increased fluorescent intensity rations between 340nm over 440nm and 340nm over 460nm using 280nm excitation in breast carcinoma biopsies [60]. The changes of the ratios were due to the fluctuations of the tryptophan and NADH concentrations which were correlated with histological tumor grades determined by pathologist [61]. Reinhold *et al*. reported a stepwise two-photon excited method to specifically excite melanin with 810nm nanosecond laser pulse [62]. Without the interference of other endogenous fluorophores, the authors saw a significant melanin spectrum difference between malignant melanoma and benign melanocytic lesions. Moreover, the eumelanin and pheomelanin can be distinguished based on their emission spectrum and fluorescence lifetime [63]. In Beckman Laser Institute, melanocytic nevi were evaluated *in vivo* with the combination of TPEF and SHG. The epidermis, epidermal-dermal junction and dermis were imaged to acquire information on cell morphology and collagen structures. Common nevi without dysplastic changes, dysplastic nevi with structural and architectural atypia, and melanoma were distinguished quantitatively [64]. Even with SHG alone, the remodeling of ECM by epithelial cancer cells can be evaluated from the collagen polarization with the help of Fourier transform or curvelet transform [65, 66].

2.1.3 Optical redox ratio

In the list of endogenous fluorophores, reduced nicotinamide adenine dinucleotide (NADH) and oxidized flavin adenine dinucleotide (FAD+) attracted our attention. As shown in figure 1, when the cells are more oxidative, the cells will reduce the FADH2 to FAD+; and when the cells are more glycolytic, the cells will oxidize the NAD+ to NADH. Two photon excited fluorescence (TPEF) microscopy has been investigated for its potential in quantify cellular metabolism by assessing the intrinsic fluorescence originating from two fluorescent cofactors NADH and FAD+ [67].

Since the first publication by Chance et al. [68], the ORR has been used in a broad range of applications spanning from cancer detection and diagnosis, predicting drug response, and monitoring cellular function and stem cell differentiation [69-73]. Unlike competing quantitative techniques with which the cells have to be lysed [74-76], TPEF microscopy provides a nondestructive, real-time and label-free method for quantifying cellular metabolism. It enables the spatial mapping of metabolic rate at the sub-micrometer scale with minimum interruption to normal cell function [77, 78].

2.2   Raman Microscope

2.2.1 The Raman effect

All the light-matter interaction happens either by absorption or scattering. When the incident photon hit a molecule, the photon can be absorbed and the energy will be completely transferred to the electrons if the energy matches the energy gap of the molecule. Thus, only the photons with specific wavelengths can get absorbed and the

absorption spectrum can be used to characterize chemical composition. However, scattering is a bit more complicated. When the particle is smaller than the wavelength of the photon or the medium is heterogeneous, the emitted photon is of the same energy as the incident photons. This is called Rayleigh scattering whose scattering intensity is proportional to λ^{-4}. On the other hand, the emitted photons can have different energy as the incident photons which is called inelastic scattering. The energy of the emitted photons can be either larger (blue-shift) or smaller (red-shift) than the incident photons and the energy differences is related to the molecular vibrational states.

Raman effect is one kind of inelastic scattering and was first observed by C.V. Raman and K.S. Krishan in 1928 [79]. They used focused sun light and observed a mixture of elastic and inelastic scattering events. Most of the photons preserved their energy and only a very small portion presented the energy shift. The Raman signal intensity is extremely low and only 1 in 10 million photons would go through spontaneous Raman scattering. In order to generated detectable signal, powerful laser source was usually used and the integration time was kept high to increase signal to noise ratio.

Different molecules have different vibrational frequencies and enable us to examine the chemical composition with the Raman spectroscopy (table 2.2). Moreover, spontaneous Raman signal is linearly proportional to the number of oscillators in the probing volume and makes it good for quantitative analysis. Haka *et al.* reported the utilization of Raman spectroscopy system for margin assessment during breast surgery based on the change of lipid composition and stromal alterations [80]. The use of Raman imaging technique has also been found in various cancer types [81-85].

chemical bonds	description	Raman peaks (cm^{-1})
OH	Bonded/unbonded hydroxyle groups	>3400
C=C	lipid saturation	~3015
CH3	DNA	~2956
CH2	Protein	~2931
CH2	lipid	~2854
C=O	aldehyde, carboxylic acid and ester bonds	~1730
C=C	amide I	~1684
C=C	aromatic componds	~1660
C=C	tryptophan	~1550
CH	collagen, lipid	~1447
CN	Amide III, collagen	~1265
CH	Tyrosine	~1176
CN	protein	~1084

Table 2.2 Chemical bonds and their corresponding Raman peaks [86, 87].

2.2.2 Coherent Raman Scattering (CRS)

Since all the oscillators vibrate independently, spontaneous Raman scattering is rather incoherent and makes the collection of the low signal even harder. To compensate for that, the system need to use either high laser power or long integration time which neither are preferred on a biological sample.

However, Maker and Terhune demonstrated that coherent Raman signal with more than 5 orders of intensity can be obtained by using two coherent laser beams to drive a vibrational Raman mode [88]. When the difference of the pump beam (ω_p) and the Stokes beam (ω_S) frequencies matches with the vibrational Raman mode, the nuclear

mode can be driven efficiently. Moreover, the coherent summation of the radiating polarization makes the emitting photons travels in certain directions only. The gain of signal intensity and directionality makes the coherent Raman imaging more applicable for biomedical applications. Both laser beams need to be spatially and temporally overlapped which is controlled either electronically by a computer or optically by an optical parametrical oscillator.

Coherent anti-Stokes Raman scattering (CARS) and stimulated Raman scattering (SRS) are the two most frequently used CRS (figure). CARS is a four-wave mixing process and makes the Raman signal scales quadratically with the pump intensity, linearly to Stokes intensity and quadratic to the number of scatters. After the light-matter interaction, a photon with $2\omega_p$-ω_S can be detected. On the other hand, SRS is emitted at the same frequency as the incoming Stokes beam. It can be considered as an energy transfer from the pump beam to the Stokes beam [89]. The signal can be extracted either from the pump beam (stimulated Raman loss) or the Stokes beam (stimulated Raman gain). For fast imaging, the pump beam is usually amplitude modulated with 100% modulation depth (figure 2.1). The phase relation between the incident pump beam and output Stokes beam signal can be analyzed with lock-in amplifier to determine the SRS signal intensity [90]. Unlike CARS, SRS signal is linear to the molecule concentration and does not present a non-resonant background.

2.2.3 Hyperspectral imaging

The CRS has a clear advantage over the spontaneous Raman scattering as it has stronger signal intensity and coherent emission. However, the CRS can only probe one vibrational

frequency with specific pump and Stokes beam combination while spontaneous Raman

can collect the whole spectrum with single excitation. In order to acquire the full

spectrum information, different ω_p-ω_S need to be probed in the same location. Fa-Ke *et*

al. used a grating based pulse shaper to get multiple wavelengths from a femtosecond

laser beam (pump) and used a narrowband ps laser (Stokes) to get high spectral resolution

[91]. If a particular chemical species is of interest, Christian *et al.* reported a spectrally

tailored excitation system that probes multiple vibrational bands simultaneously [92].

To achieve the spectra scan capability and avoid system complexity, we swept the

pump beam across the interested spectrum region by adjusting the crystal temperature,

lyout filter and cavity length of the OPO. The spectral scan was controlled by a

customized software following the steps: tuning the pump frequency, adjusting the power,

acquire an image, calculate the next pump frequency and repeat. As shown in figure 2.2,

the pump beam can be adjusted to probe the lipid, protein and lipid saturation regions

discretely to quantitatively evaluate the sample chemical composition. If the wavelength

of the pump beam is tuned continuously, the molecule spectrums of each individual

pixels can be plotted in any Raman region. Moreover, the data can be analyzed with

vertex component analysis to separate different molecules based on their spectrum [93].

The image in figure 2.2c demonstrated a live sample with three major components (lipid,

protein and water).
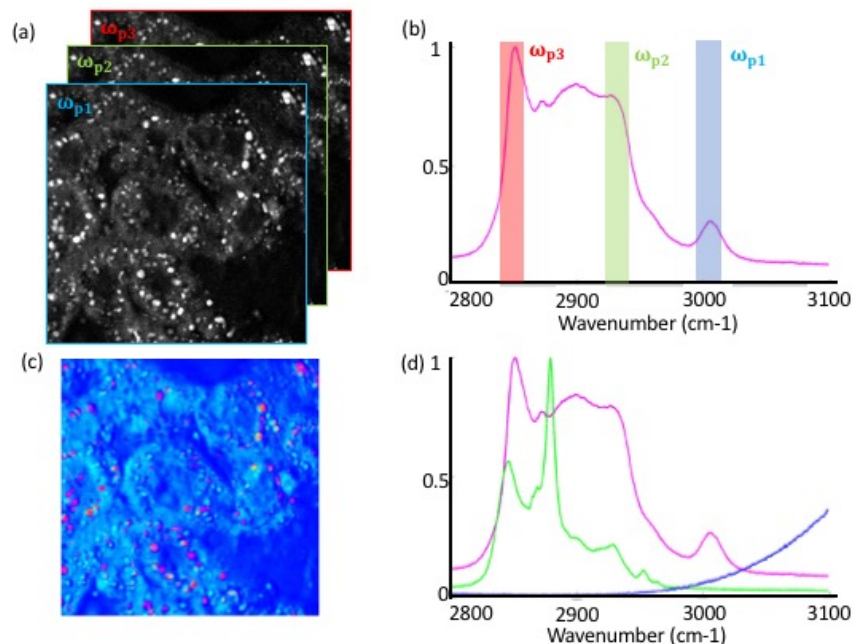
Figure 2.2. Hyperspectral scan. (a) the images taken at three different wavelengths; (b) the pump beam was adjusted to probe the lipid, protein and lipid saturation; (c) pseudo color images of liver sample with red pixels represent lipid, green pixels represent protein and blue pixels represent water.

2.2.4 Deuterium labeling

Advanced optical microscopy methods offer a solution by offering a direct view of the cell with high spatial resolution and at high image acquisition rates. Yet, fluorescent labeling, which is the most common contrast mechanism, is not an attractive option for following carbon flow, because fluorescent labels are not suitable for following individual chemical groups as they undergo chemical conversion [94, 95]. Label-free techniques, such as vibrationally sensitive stimulated Raman scattering (SRS), generate contrast from endogenous chemical groups [96, 97]. However, the palette of distinct vibrational modes is limited, and chemical units of interest are difficult to discriminate from the signal derived from other endogenous compounds. Recently, deuterium

labeling has regained popularity in Raman based imaging for singling out compounds of interest against the background. Deuterium labeling shifts the resonances of chemical group vibrations to regions of the vibrational spectrum devoid of overlapping Raman modes, enabling a virtually background-free detection of the targeted chemical groups. Moreover, the bioactivity of deuterated compounds is often indistinguishable from the bioactivity of non-deuterated analogues, confirming that the cellular machinery is virtually unaffected by the additional neutron on the hydrogen nuclide. For instance, deuterated amino acids have been used to follow active protein synthesis in live cells, indicating that the deuterated amino acids analogues are incorporated by the cell in a non-perturbed fashion [98]. Previous Raman imaging studies have shown that the movement and incorporation of small deuterated molecules can be monitored in live cells. However, it is unclear if the same strategy can be employed to track chemical information through a multi-step conversion process, whereby the individual chemical groups of supplied nutrients are disrupted and incorporated into completely different structures.

In this study, we push the principle of deuterium labeling one step further for the purpose of following the flow of hydro-carbon chemical groups in a living system. We supplied cells with fully deuterated glucose and followed glucose consumption for de novo lipid synthesis in an ER positive breast cancer cell line (MCF7) and in primary mammary epithelial (PME) cells. Using spontaneous Raman and SRS spectral imaging, we observed the formation of metabolic products of glucose and the accumulation of hydro-carbon units derived from glucose inside lipid droplets in cancer but not normal

cells. SRS microscopy probes different chemical vibrations by adjusting the optical frequency difference between two incident laser beams (pump and Stokes). In our experiment, we kept the optical frequency of the Stokes beam constant and tuned optical frequency of the pump beam to image both natural aliphatic lipids (Raman shift is 2850 cm^{-1}) and deuterated hydro-carbons (Raman shift is 2175 cm^{-1}). The MCF7 breast cancer cells are cultured in medium with either deuterated glucose or regular glucose.

Chapter 3

Sample preparation and data analysis

3.1   System set up

The system configuration is illustrated in figure 3.1. CARS and SRS imaging modalities
are integrated into the Olympus IX71. A 76-MHz mode-locked Nd:Vanadate
laser(picoTrain, High-Q) was used to deliver a 7-ps pulsed laser beam at 1064nm (Stokes
beam) and a second harmonic generated beam at 532nm to pump an optical parametric
oscillator (OPO; Levante, Emerald OPO, Applied Physics & Electronics Inc.). The
OPO generated the corresponding pump beam for imaging either the normal lipid
distribution (817nm) or deuterated signal (864nm) by adjusting the crystal temperature,
Lyout filter and cavity length. The Stokes beam was modulated by 10MHz with an
acousto-optic modulator (12465 , Crystal Technology Inc.) and, then, spatially and
temporally overlapped with the pump beam before sending into a laser scanning
microscope (IX71, Olympus). The cells were imaged by a 60X water objective (1.2NA,
UPlanSApo, Olympus) and the stimulated Raman loss of the pump beam was collected in
the forward direction by a high NA condenser (). The CARS and SRS signals were
separated with a dichroic mirror. The CARS signal was detected by a Hamamatsu

photomultiplier tube (R2658, Hamamatsu) with a 650 +/-50nm bandpass filter in front.

The Raman loss in the pump beam was detected by a photodiode (FDS1010, Thorlabs)

and a high O.D. bandpass filter (Semrock) was placed in front of the photodiode to block

the Stokes beam. The modulated signal from the photodiode was filtered with an

electronic bandpass filter (BBP-10.7+, Mini-Circuits) to suppress the 76-MHz signal

from laser pulsing and low frequency signals from scanning. The filtered voltage signal

was demodulated by a homemade lock-in amplifier and sent to the computer for display.

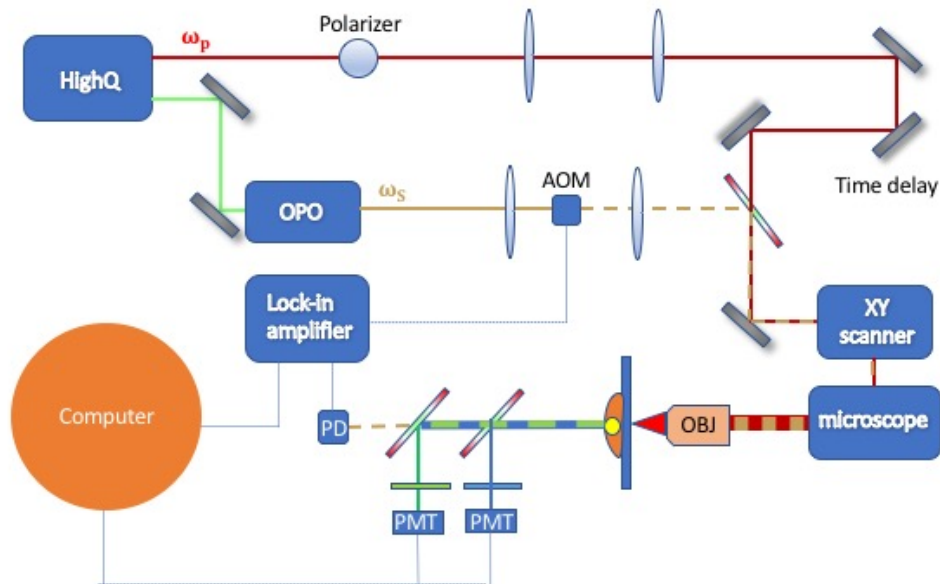**Figure 3.1.** the scheme of multi-modal imaging platform. OPO: optical parametric oscillator; AOM:
acousto-optic modulator; PD: photodiode; PMT: photomultiplier tube; Obj: objective.

For all imaging, 512 by 512 pixels are acquired for one frame with 10 μs pixel

dwell time. The average laser power on the sample was kept constant at 15mW for the

Stokes beam. For the pump beam, we used 15mW for imaging normal lipid distribution

(817nm) and 20mW for imaging deuterated signals (864nm) to minimize sample photodamage. We also took an off-resonant image (pump 890nm, 35mW) for each individual measurement.

The cellular redox states and SHG signals were measured on a commercial Zeiss laser scanning microscope (LSM510) equipped with a femtosecond laser source (Chameleon, Coherent Inc.). The laser beam was focused onto the cells through a 40X water objective. The fluorescent signals and SHG signals were collected in the epi direction. The fluorescence of NADH was excited at 740nm and collected with 480nm±50nm bandpass filters in front of the photomultiplier tube (PMT). Then, we used 900nm excitation and detected the fluorescence of FAD+ at 530nm±50nm and SHG signals of collagen fibers at 450nm±10nm. All the images were taken with 512 by 512 pixels with 6 μs pixel dwell time. We used 10mW at the sample for NADH imaging and 15mW for FAD+ imaging. To calibrate the environmental and system vibrations at different dates, we acquired images of a freshly-prepared fluorescein solution (0.02 μM at pH7) as a reference.

For hyperspectral SRS Imaging, the region of interest was identified with regular SRS imaging. The pump laser wavelength was tuned from 803nm to 820nm (0.3nm stepwise) by computer control of the crystal temperature, Lyout filter and cavity length of the OPO [99]. The laser power was monitored by a photodiode detecting the reflection from a cover glass before the scanner box. The power was kept constant for all the wavelengths throughout the experiments. After the scanning process, we obtained an imaging stack that contains the Raman spectrum information for each pixel from 2791cm-1 to 3055cm-1.

The spontaneous Raman spectra were acquired with a commercial Raman microscope (InVia Confocal, Renishaw) at room temperature. A 532nm diode laser was focused onto the sample through the 60X water objective (1.2NA, UPlanSApo, Olympus). The laser power was kept at 12mW and the exposure time was 40s in order to get the spectrum from 500cm-1 to 3200cm-1. All the spontaneous Raman spectra were smoothed with Savitzgy-Golay algorithm and the backgrounds were subtracted with polynomial fitting. The data processing was done in Matlab.

3.2   Sample preparation

Deuterated glucose (552003), normal glucose (G7021), l-arginine (A5006), l-lysine (L5501) and 17β-estradiol (E8875) were purchased from Sigma-Aldrich. SILAC Advanced DMEM/F-12 flex media, no glucose, no phenol red (A2494301), TrypLE (12604013), charcoal stripped fetal bovine serum (12676011), Hanks buffer (14025092) and glutaMAX (35050-061, Life Technologies) were purchased from ThermoFisher scientific. Mammary Epithelial Cell Basal Medium (PCS-600-030) and growth kit (PCS-600-040) were purchased from ATCC. Matrigel (356231) and high concentration rat tail collagen I (354249) were purchased from Corning.

Advance DMEM/F-12 culture medium was made by adding 5% charcoal stripped FBS (vol/vol), 1% glutaMAX (vol/vol), 147.5 mg/L l-arginine, 91.25 mg/L l-lysine and 3151 mg/L normal glucose. Serum free medium was made as advanced DMEM/F-12 culture medium without FBS. Deuterated culture medium was made by replacing normal glucose with 17.5 mM deuterated glucose. 17β-estradiol was dissolved in DMSO with 10-8 M.

PME, T47D, and MDA-MB-231 were obtained from American Type Culture Collection (ATCC). The PME cells are cultured with Mammary Epithelial Cell Basal Medium added with growth kit. Both MDA-MB-231 and T47D breast cancer cells obtained from ATCC were cultured at 37 °C and 5% CO2 in advanced DMEM/F-12 culture medium. The culture medium was regularly changed every two to three days to remove waste and provide the cells with fresh nutrients to grow. The cells were monitored on a daily basis and washed and passaged at 80% confluency. For all the experiment, cells were washed three times with Hanks buffer and detached from flasks using TrypLE. We collected all the cells, centrifuged and resuspended in regular culture medium and counted with a hemocytometer.

To make the 3D breast cancer model, Matrigel was thawed on ice for 12 hours before the experiment. The pipet tips and imaging dishes (7160-2, Miltenyi Biotes) are chilled in -20 ˚C overnight. The high concentration rat tail collagen I was diluted to 3.2mg/ml by following the manual provided on the website. Both the matrigel and collagen were mixed with 1:1 ratio to match up with the mechanical properties of extracellular matrix. Imaging dishes were coated with 50ul matrigel/collagen mixture and left in the incubator for 1 hour to become solidify. Cells were detached from plates using TripLE, stain with trypan blue and counted with a hemacytometer. The experiment would continue only if the cell live rate was above 90%. The cells were collected and gently pelleted by centrifugation at 1000rpm for 8 minutes. The medium was aspirated and the cells were suspended in 500ul matrigel/collagen mixture and plated onto the coated imaging dishes. The plating cell concentrations were 100k/well for PME cells and 60k/well for T47D and MDA-MB-231 cells. The dishes were put in the incubator for an

hour to gel before adding 2ml culture medium. The cells were incubated at 37 ˚C, 5%
CO2 and the medium is changed every three days. For each cell lines, three identical
imaging dished are prepared. To introduce cancer invasiveness in T47D cell lines, 10-8
M 17β-estradiol was added to the culture medium.

3.3   Metabolic Measurements

Metabolic measurements of the acini. The power of the laser and the gain on the PMTs
were kept constant for all the measurements during the experiments. Before the metabolic
measurements, the fluorescein and olive oil were imaged as reference samples for TPEF
and CARS respectively. The glucose and lipid metabolic changes were measured every
other day for 12 days. For glucose metabolism, we first excite NADH with 740nm
excitation wavelength, then, tuned to 900nm to measure the concentration of FAD+ at the
same planes. The lipid content was measured with CARS. Same acinus structure was
identified using the coordinates etched at the bottom of the gridded imaging dish.

To track the metabolic changes during the acini formation, fifteen different PME
acini structures were randomly chosen from each imaging dish. The entire 3D volume of
acinus structure was imaged with 1um step size for both glucose and lipid metabolism.
To compare the metabolic signatures of PME, T47D and MDA-MB-231 cells, 15 acini
from each group were imaged after 12 days of culturing. The redox ratio and lipid content
of each acinus was calculated as described in detail later. To study the metabolic changes
in response to E2, we added 17β-estradiol (10-8 M) to both PME and T47D 3D culture.
The metabolisms of 10 randomly chosen acini were measured before adding E2 and 3
days after adding E2.

Lipid synthesis from deuterated glucose. The cells were seeded on round coverslips in 24-well plates at 50,000 cells/well with 1mL advanced DMEM culture medium. For the first experiment that tested the system's capability to visualize the deuterated carbon flow, 6 wells of the cells were switched to deuterated culture medium and another 6 wells of the cells were switched to fresh normal culture medium. The cells were cultured at 37°C and 5% CO2 for 24 hours before imaging.

For lipid dynamic studies, the advanced DMEM culture medium was changed to serum free medium for cell cycle synchronization for 12 hours. After synchronization, the control groups (6 wells) were replaced with deuterated culture medium and DMSO and the experimental groups (6 wells) were replaced with deuterated culture medium and 17β-estradiol (10-8 M). After 24 hours of culturing, we switched all the wells to normal advanced DMEM/F-12 culture medium (considered T=0). We fixed one well of control group and experiment group at times T=0h, 3h, 6h, 9h, 12h and 24. For the experiment that studied the correlation between glucose metabolism and lipid synthesis rate, 6 imaging dishes of cells were prepared. All the cells were changed to serum free medium for cell cycle synchronization for 12 hours. After synchronization, all the dishes were washed. We added deuterated culture medium with vehicle control to 3 imaging dishes and deuterated culture medium with 17β-estradiol (10-8 M) to the other 3 dishes. The cells were cultured at 37°C and 5% CO2 for 24 hours and imaged with TPEF following SRS imaging. The temperature of the culture medium was kept constant at 37°C to get accurate measurements on the cellular redox states. In all the experiments, five locations were randomly imaged in each well or imaging dish.

3.4 Quantitative analysis

The fluorescent intensities of NADH and FAD+ were calibrated with the fluorescein reference sample as,

$$I_{cali} = (I - I_{min}) * \frac{I_{ref}}{I_{ref1}}$$

in which, I_{cali} is the calibrated signal, I is the direct measured signal intensity, I_{min} is the minimum intensity in the image, I_{ref} is the mean intensity of the fluorescein sample measured before the experiment and I_{ref1} is the mean intensity of the reference sample measured at day 1.

For TPEF images, the background noise, cytoplasm, and cell nucleus wre separated by the three component Otsu algorithm. The redox ratio (FAD+/(NADH+FAD+)) was calculated in the cytoplasm regions pixel by pixel. For 3D experiments, the redox ratios of all cells in the entire 3D volume were averaged and stored as a representative redox ratio for the whole acinus. And for 2D experiments, the redox ratios of all cells in the field of view were averaged. Lipids are detected based on their CARS intensity. A four component (background, cell nuclei, cytoplasm and lipid droplets) Otsu thresholding algorithm was used to get the area of cytoplasm. We use the number of pixels of lipid droplets over the number of pixels of cytoplasm to estimate the lipid percentage.

In Matlab, we first did fast Fourier transform to all the SRS images to get rid of background noises. Then, we removed nonspecific signals by subtracting off-resonant SRS images from SRS images of normal lipid distribution and deuterated signals. The processed images were exported and saved as TIFF files. The background-subtracted

normal lipid SRS images and the matching deuterated lipid SRS images were opened in ImageJ. We manually selected out the lipid droplets and used the average intensities within the regions of interests to calculate the dLD/LD ratios. Fifteen to twenty different droplets were analyzed in each field of view and fifty droplets were included for statistical analysis for each group.

For hyperspectral SRS stacks, we used vertex component analysis (VCA) to retrieve the three most prominent spectral features from the images. The VCA algorithm was written with Matlab and discussed in detail in [100]. The three main spectral components were identified as end members and were assigned different colors (red, green and blue in this case). Each hyperspectral cube of each pixel was fitted with linear combination of the three components and given a corresponding RGB color. The redox ratio and lipid percentage measurements during the acini formation were tested with linear mixed model to validate the increasing trend of metabolic rate at different days. The metabolic measurements between different cell lines and before and after drug treatments were tested with two components ANVOA tests. A significance level less than 0.05 were used for all statistical analysis.

Chapter 4

Correlating optical redox ratio with normalized cellular oxygen consumption

4.1 Introduction

Because of their role in mitochondrial electron transport, the relative fluorescence

intensity of NADH and FAD+, defined as the "optical redox ratio (ORR)", can be used to

estimate the contribution of oxidative phosphorylation versus glycolysis in cellular ATP

production [101, 102].

However, quantifying and interpreting the ORR is challenging. The measured

fluorescence intensity overlaps with the emission of additional fluorophores. NADPH

and NADH, in particular, have similar excitation and emission spectra and cannot be

differentiated easily [103]. Moreover, the fluorescence quantum yields of NADH and

FAD+ are affected by their binding state to other metabolic enzymes [104, 105]. In order

to test the robustness of the ORR for measuring cell metabolism, a number of studies

have attempted to validate the correlation between ORR and the oxidation-reduction ratio

of NAD+/NADH [29, 106]. Among them, Kyle et al. [107] used liquid

chromatography/mass spectrometry and found that while the fluorescence intensities of

FAD+ and NADH are not correlated with their actual intracellular concentrations, the

ORR is significantly correlated with NAD+/NADH. However, no work has been reported to evaluate the stability and accuracy of ORR in living, dynamic biological samples.

4.2 Experiment details

In this work, we use TPEF to measure ORR in living MDA-MB-231 breast cancer cells under normal culture conditions and in MCF7 breast cancer cells to dynamically measure metabolic changes in response to a series of mitochondrial inhibitors and uncouplers (oligomycin, carbonyle cyanide-4-phenylhydrazone (FCCP) and rotenone/antimycin A). The ORR, defined as FAD+/(NADH + FAD+), was calculated from dual wavelength excitation TPEF images, as discussed below. TPEF results were compared to seahorse flux analysis (Seahorse XFe24, Seahorse Bioscience) of the cellular oxygen consumption and proton production rates (OCR and PPR, respectively). Seahorse flux analysis is a standard metric that directly reflects average cell oxidative phosphorylation and glycolysis rates [108]. To compare results from the Seahorse flux analyzer to the ORR, we used a normalized oxygen consumption rate (defined as n-OCR = OCR/PPR) for all our analyses.

MDA-MB-231 and MCF7 breast cancer cells were cultured in SILAC DMEM flex medium (A2493901, Life Technologies) supplemented with 6mM glucose, 0.85mM L-arginine and 0.6mM L-lysine, 5% fetal bovine serum and 1% glutaMAX (35050-061, Life Technologies). Cells were detached from plates using 2% EDTA in 1x PBS, counted with a hemocytometer and then plated 16 hours prior to experiment. We plated 80,000 cells/well in XF24 cell culture microplates (#V7-PS, Seahorse Bioscience) for Seahorse analysis and 50,000 cells/dish on imaging dishes (fd35-100, World Precision Instrument)

36

for ORR measurements. An hour ahead of the Seahorse experiment, cells were washed twice with 1 mL of XF Base Medium (#102353-100, Seahorse Bioscience) before adding 450 µL XF complete Medium (Base Medium + 25mM glucose + 2mM glutamine + 1mM sodium pyruvate) and incubated at 37 °C with 0% CO2. Standard protocols for Seahorse flux assay calibration and analysis were employed. All Seahorse flux data were normalized to total protein content measured by BCA Assay (#23225, Thermo Scientific) at the end of the experiment, assuming tight correlation between the protein content and cell numbers per well. The ORR of the cancer cells was measured with a commercial Zesis LSM510 microscope equipped with a tunable ultrafast laser source (Chameleon, Coherent Inc.). In each dish, three locations were randomly selected and imaged. The fluorescence of NADH (excited at 740nm and collected at 380nm±50nm) and FAD+ (excited at 900nm and collected at 530nm+/- 50nm) was excited and collected in the epi direction sequentially. Two dishes were prepared for each cell line. We used 1 µM Oligomycin, FCCP, and Antimycin A/Rotenone in sequence on live MCF7 cells and studied the dynamic changes of cell metabolism by the ORR and Seahorse flux analysis on individual cell lines employing the same protocol. Both ORR and normalized oxygen consumption rate (n-OCR) were acquired every 5 minutes for a total of ten measurements in 45 minutes. Following baseline measurements (T=0), Oligomycin was added and three measurements were performed (T=5, 10, 15). FCCP and Antimycin A/Rotenone were added in a similar manner, right after T=15 and at T=30, respectively, and following completion of three ORR/n-OCR measurements. Identical image planes and constant laser power were maintained for all measurements. We used a freshly-prepared fluorescein solution (0.02 uM at pH7) as a reference sample for calibrating all

measurements. The image intensities were adjusted based on the fluorescein reference images and analyzed with ImageJ. The region of the cytoplasm of each cell was manually selected to calculate the ORR and compared to the normalized oxygen consumption rate measured by flux analyzer. For statistical analysis, we included the data from 12 wells for the flux analyzer (approximately 50,000 cells/well and 3 wells for each cell line) and 25 cells for optical redox ratio.

4.3 Results and discussion

Figure 4.1 shows typical images of NADH (1a) and FAD+ (1b) of MDA-MB-231 cells in the same field. Average intensities within the cytoplasm region of interest (ROI) were used to calculate the ORR. Both Seahorse flux analyzer (n-OCR) and ORR showed higher oxidative phosphorylation rates for MDA-MB-231 cells vs MCF7 cells (tested with two-tailed ANOVA, $p<0.05$) (Figure 1c). Similar observations for these two cell lines were reported by Walsh et al. using fluorescence lifetime based ORR estimates [29]. Differences in ORR are likely due to the cancer phenotype; highly metastatic MDA-MB-231 cells have relatively high mitochondrial biogenesis and oxidative phosphorylation rates mediated by PGC-1α [16].
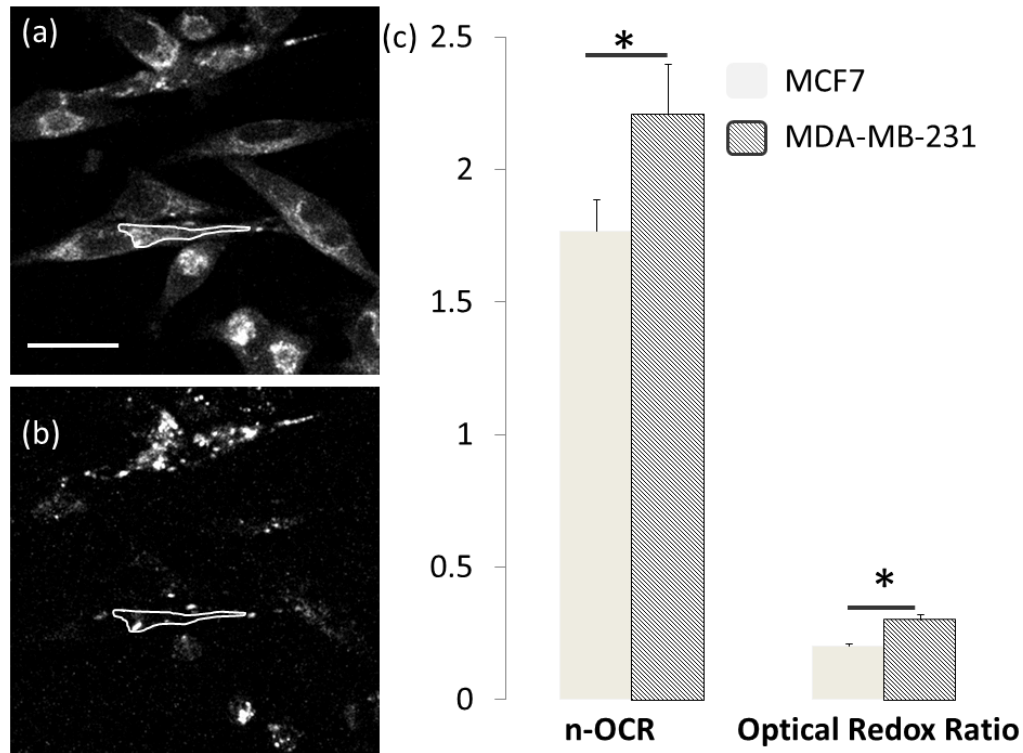
Figure 4.1. Metabolic measurements of tumor cells under normal culture conditions. (a) TPEF of MDA-MB-231 cells, NADH channel; (b) TPEF of MDA-MB-231 cells, FAD+ channel. The outlined region of interest (ROI) selects cellular cytoplasm for calculation of the optical redox ratio (ORR). (c) Normalized oxygen consumption rate (n-OCR) and the ORR for MCF-7 and MDA-MB-231 cells. The measurements from each cell line are compared with two-tailed ANOVA. Both measurements demonstrate statistically different metabolic rates for MCF7 cells and MDA-MB-231 cells ($p<0.05$). The error bars for n-OCR come from the standard deviation of 12 different wells (50,000 cells/well) and the error bars for ORR come from measurements on 25 different cells.

Figure 4.2 shows the metabolic response of MCF7 cells to the mitochondrial inhibitors and uncouplers measured by both TPEF and seahorse flux analysis. The ORR changes are similar to the n-OCR ratio measured independently with Seahorse experiments. After adding oligomycin, the cell mitochondrial proton channels are

blocked and energy is provided primarily by glycolysis. The inhibition of oxidative

phosphorylation is reflected by the substantial reduction in n-OCR and ORR. The

subsequent addition of FCCP uncouples ATP synthesis from electron transport and

recovers the cells from the effects of oligomycin. Both n-OCR and ORR return to values

that are close to baseline. Finally, Rotenone/Antimycin A was added to stop the passing

of protons to Coenzyme Q (CoQ), completely shutting down oxidative phosphorylation

and dropping n-OCR and ORR to their lowest levels.
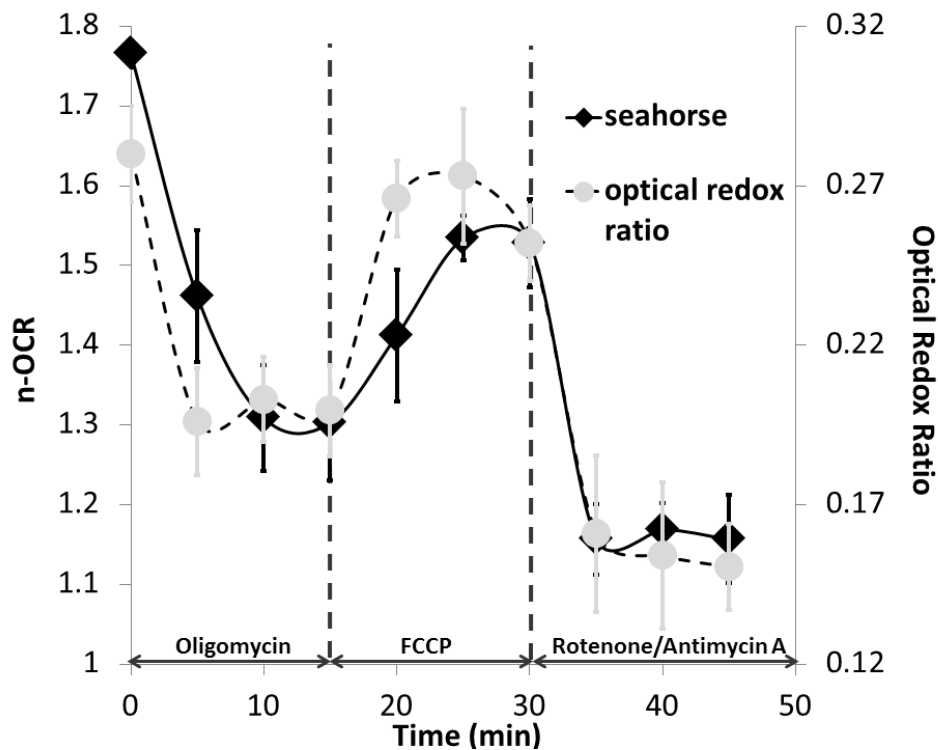
Figure 4.2. Dynamic monitoring of MCF7 cell metabolism by TPEF microscopy (circles, dashed line) and

Seahorse flux analyzer (diamonds, solid line). Cells in regular culture conditions were measured at time 0

and then treated with Olygomycin, FCCP and Rotenone/Antimycin A at T = 0, 15 and 30 minutes in

sequence. The n-OCR and ORR were measured every 5 minutes. The error bars for n-OCR come from the

standard deviation of 12 measurements and the error bars for ORR come from measurements on 25

different cells.
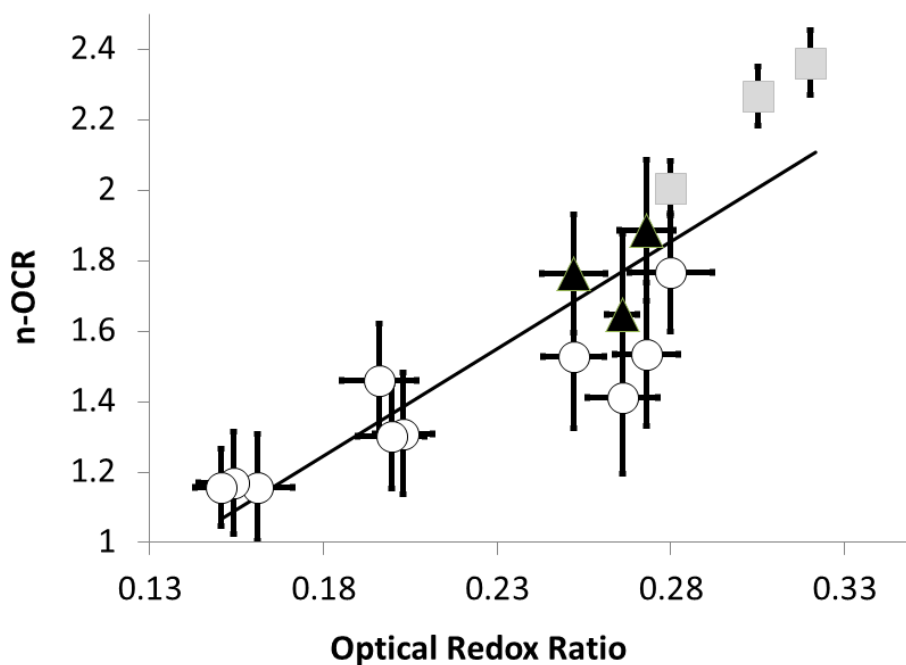
Figure 4.3. The ORR is significantly correlated with the n-OCR (R=0.7901, p<0.001). The circles are from the dynamic study of MCF7 cells, the squares and triangles come from the measurements of MDA-MB-231 and MCF7 cells, respectively, under normal culture conditions. The black line is the general linear fit with all the data points. Each data point represents an average value from 12 flux analyzer measurements and 25 cells from TPEF. The error bars are calculated as the standard deviation of corresponding measurements

To evaluate the correlation between the ORR and n-OCR, we pooled the data acquired from measurements of the two cell lines under both static (Figure 4.1) and dynamic (Figure 4.2) conditions and evaluated it using a linear regression model (Figure 4.3). Elevated ORR values are correlated with higher cellular n-OCR. Under these conditions we expect that the relative contribution of oxidative phosphorylation to cellular energy production would be higher than that of glycolysis. A decrease of ORR

implies a metabolic shift from oxidative phosphorylation towards aerobic glycolysis in cancer cells. And in our experiments pure anaerobic glycolysis under Rotenone/Antimycin A treated condition is accompanied by the lowest n-OCR and ORR. The overall correlation is highly significant (R=0.7901, p<0.001).

4.4   Concluding remarks

In summary, we demonstrate that the ORR derived from dual wavelength TPEF of intrinsic NADH and FAD+ cofactors strongly correlates with Seahorse flux analysis of the cellular metabolic rate of oxygen consumption. Our results, obtained from two different breast cancer cell lines under both static conditions and dynamic perturbations of mitochondrial function, suggest that the ORR is a simple yet robust imaging index of cancer cell metabolism that can be used across a broad range of oxygen consumption conditions.

Chapter 5

Monitor metabolic response in 3D breast cancer model

5.1   Introduction

Despite the generality of the Warburg effect, determination of the glycolytic rate in cells alone is often insufficient to classify cell malignancy. This is because normal cells can also present a high rate of glycolysis as regulated by environment, cell function and endocrine factors [109, 110]. For example, endothelial cells display a high glycolytic rate when phosphofructokinase-2/fructose-2,6-bisphosphatase3 (PFKFB3) activity is high, which is known to correlate with its antigenic capacities [111]. Insulin can also affect cellular glucose metabolism through sterol responsive element binding protein-1c (SREBP-1c) [112].

To improve the assessment of cellular health in the context of its glycolytic rate, glucose metabolism can be correlated with other metabolic observables in the cell. In many cancers, including breast cancer, metabolic reprogramming benefits biomolecule synthesis to meet the high demand of biomass for mitosis. In mammary epithelial cells, an important end product of cellular biosynthesis is milk fat [113]. It is well known that breast cancer is associated with altered lipid metabolism, which is manifested in changes in intracellular lipid quantities [114]. Correlating the cellular glycolytic rate to lipid metabolism in breast cells thus represents an improved strategy for assessing cell

malignancy based solely on metabolic observables. Importantly, both glucose and lipid metabolism can be monitored with label-free optical microscopy techniques, offering a route to assess cellular health *in vivo* in a potentially non-invasive manner.

In this work, we use multi-modal nonlinear optical microscopy to characterize both glucose and lipid metabolism in normal and breast cancer cells. By correlating several complementary NLOM intrinsic signals, we show that diseased cells can be differentiated from normal cells, and that their level of invasiveness can be charted. Specifically, we employ two-photon excitation fluorescence (TPEF) to determine the cell's glycolytic rate as reported by the ratios of metabolic coenzymes (FAD^+/(NADH+ FAD^+)) [115-117], and coherent Raman scattering (CRS) microscopy [99, 118-120] to probe intracellular lipid content and *de novo* lipid synthesis. In addition, we map the extracellular matrix (ECM) in 3D organotypic tissues by visualizing second harmonic generation (SHG) signals from collagen, a major component of ECM [121].

The combination of these imaging techniques enables the evaluation of glucose and lipid metabolism in live cells with minimum interruption. We examine metabolism in primary mammary epithelial (PME) cells, and in two lines of breast cancer cells, T47D and MDA-MB-231 cells. To mimic the conditions in tissue, the cells are cultured in 3D in a matrigel/collagen mixture, displaying gene expression that is similar to what is seen in the body [122]. Under these conditions, the cells form physiologically-relevant acini structures. Using this platform, we show that label-free metabolic signatures can be used to fully distinguish between mature PME, T47D and MDA-MB-231 acini. We further confirm the sensitivity of the combined glycolysis/lipid metabolism metric by observing the cellular response after treatment with 17β-estradiol (E2), showing clear changes in

both cellular metabolism and ECM interactions that correlate with invasiveness. Finally, we use deuterated glucose and CRS detection [98, 123, 124] to track the flow of carbon-hydrogen units in individual cells and establish a direct link between glycolytic activity, lipid synthesis and lipid consumption. By correlating these observables, we show evidence that cancer cells respond to invasiveness stimuli with adapted metabolism, increasing both lipid synthesis and lipid consumption.

5.2   Experiment details

We used NLOM imaging to monitor the metabolic changes of PME cells during acini formation and measured the changes of redox ratio and lipid content of ten randomly chosen acini every other day for 12 days. We picked three different cell lines (PME, T47D and MDA-MB-231 cells) and cultured in 3D for 12 days. Different cell lines displayed varying morphologic features determined by their pathologic characteristics. We also measured the metabolic signatures in 3D spheroids for different breast cell lines a day 12.

5.3   Results

We used NLOM imaging to monitor the metabolic changes of PME cells during the formation of acini (fig. 5.1). Two-photon excited fluoresce (TPEF) was used to measure the optical redox ratio (ORR = FAD+/(NADH + FAD+)) while lipid content was measured using coherent anti-Stokes Raman scattering (CARS). Fifteen randomly chosen

acini were followed every other day for 12 days. Figure 5.1a-i shows ORR distributions and CARS images of cross sections of one representative PME acinus at days 4, 8 and 12.

PME cells had low optical redox ratios when first seeded into the matrigel/collagen mixture. Average ORRs started to increase but were not significantly different over the first three days. On day 4, we observed early formation of spheroids by multiple PME cells with homogeneous ORR values. From day 4 to day 10, the spheroids grew larger and the average ORR surged from 0.15 to 0.19 (p<0.01). Cell clusters started to display spatial variations in the metabolic distribution around day 8 (fig 5.1d) with ORR increasing from exterior to interior. The two distinct cell populations contributed to the observed increase in standard deviation of the mean ORR on day 8. Cell metabolism remained on the same level from day 10 to day 12. Moreover, the cells in the center that demonstrated abnormally high optical redox ratios disappeared and left a hollowed center (fig 5.1g). A single layer of PME cells formed alveolar structures that strongly mimicked normal mammary glands. ORR values in the remaining cells increased by ~50% compared to initial seeding cells.

We also observed an increase in cytoplasmic lipid content during acinus formation. Typical CARS cross-sectional images are shown in fig 5.1b, e and h. The bright spots are CARS signals from lipid droplets while the overall cell morphology can be visualized by the non-resonant CARS background. We observed near-zero lipid content in cells first seeded into the gel. However, the cells started to accumulate lipid at day 4 and the total amount of lipid droplets increased ~10 fold after another 6 days of culturing. The total lipid content reached a plateau and became stabilized after 12 days of culturing.

NLOM provided sufficiently high spatial and temporal resolution to observe coordinated changes in glucose and lipid metabolism in single cells during the process of acinus formation. A linear mixed model was used to show that both the ORR and lipid content increased significantly over time ($p<0.01$). Multiple stages of development were observed, suggesting that a minimum time is required for each acinus to become mature. For this purpose, all of the subsequent experiments were conducted on acini cultured for 12 days.
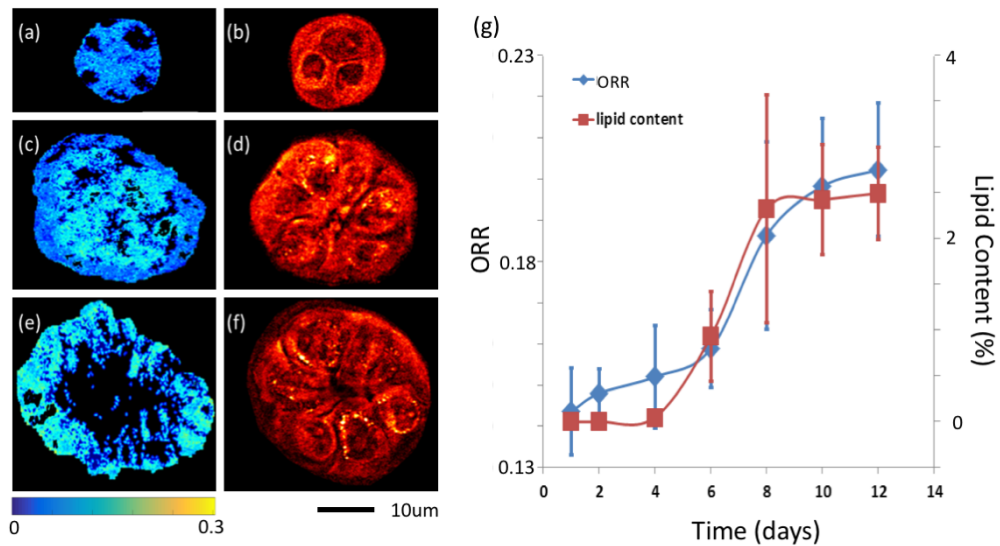
Figure 5.1. The cellular metabolic changes during acini formation. Representative TPEF **(a, c, e)** and CARS **(b, d, f)** images of the acini acquired at days 4, 8 and 12. TPEF images provide information about the redox ratio distribution inside the acini. Redox ratio of the acini structure is color coded based on the color bar on the left side. CARS images show the lipid distribution inside the acini structure **(g)** The redox ratio and lipid content of 15 randomly chosen acini structures are studied for 12 days. Each data point in the plot is an average of the 15 acini structures. The average redox ratios (diamond blue line) and lipid contents (square red line) were plot with respect to time. The error bars represent standard deviation of 15 independent measurements.

We also measured the metabolic signatures in 3D spheroids for different breast cell lines. Figure 5.2 shows TPEF images (a-c) and CARS images (d-f) corresponding to the cross sections of PME, T47D and MDA-MB-231 cells cultured in 3D on day 12. Different cell lines displayed varying morphologic features determined by their pathologic characteristics. As described above, normal cells form spheroids with a hollow center that mimic normal mammary alveolar structures (fig. 5.2a and d). However, the highly proliferative T47D ER+ breast cancer cells formed spheroid structures but with a solid center filled with cells (fig. 5.2b and e). The highly metastatic triple negative MDA-MB-231 cancer cells did not form any growth-arrested structures and spread out through the entire matrix (fig 5.2c and f).

Aside from these morphological differences, the three different cell lines had different metabolic signatures corresponding to their phenotypes. In figure 5.2g, the average ORR and lipid content of each cell line are compared. The ORR for normal breast epithelial cells (PME) was significantly higher than for the two malignant cancer cell lines (p<0.01). The ER+ T47D cell lines were the most glycolytic (lowest ORR), while the ORR for MDA-MB-231 was significantly higher than for T47D cells (p=0.013) but lower than normal. Our observations not only show that the cancer cells are more glycolytic compared with normal cells (Warburg effect) but also demonstrate that glucose metabolism can vary between breast cancer subtypes. Lipid content from the same acini was measured using CARS. All the breast cancer cell lines exhibited much lower lipid storage compared with normal breast cells. The lipid content in the PME cells was 2.5 times higher than in the T47D cell lines; and the triple negative breast cancer cells had a

lipid storage fraction close to 0 (fig. 5.2d-f). The three cell lines demonstrated dramatic differences in lipid droplet content and were well-separated with this parameter (fig. 5.2g).
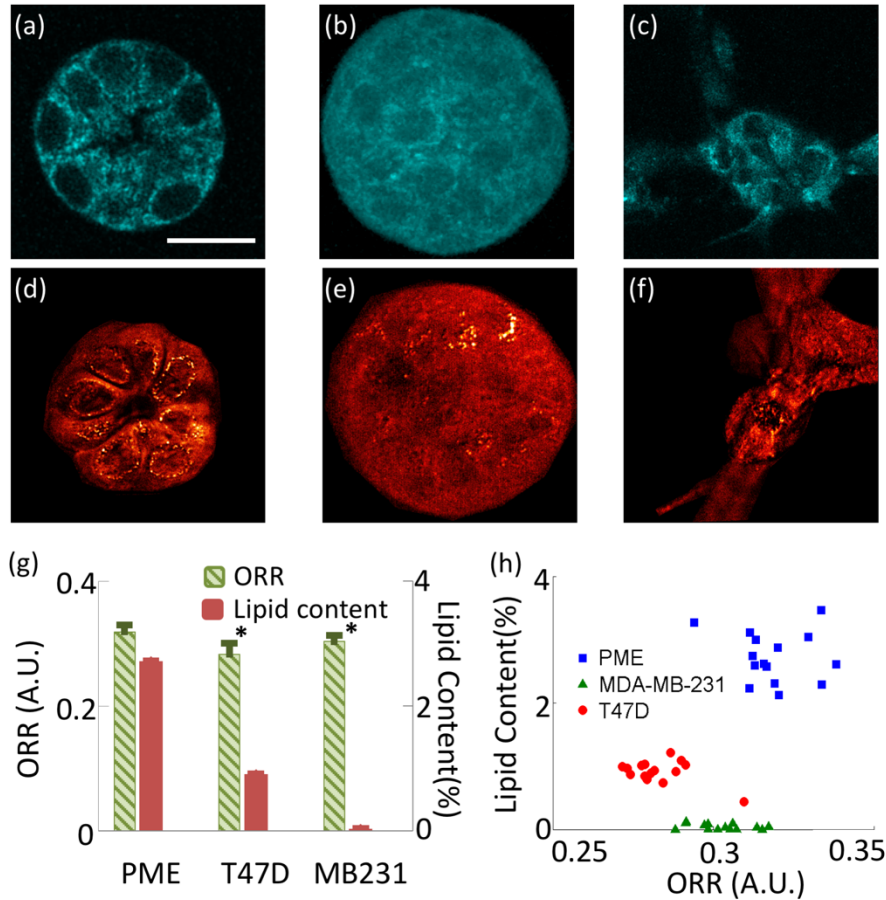
Figure 5.2. The cellular metabolic signatures of three cell lines. TPEF images of the acini cross sections of PME (a), T47D (b) and MDA-MB-231 (c) cell lines. CARS images of the acini cross sections of PME (a), T47D (b) and MDA-MB-231 (c) cell lines. (g) The redox ratio (blue) and lipid content (red) of three different cell lines are compared. Both the redox ratio and lipid content of the three cell lines were significantly different from each other. (h) The metabolic map of three different breast cell lines. PME, T47D and MDA-MB-231 cells are plot based on their redox ratio and lipid content. Each point in the metabolic map represents an average of all the cells in an acini structure. The error bars represent standard error calculated from 15 independent measurements. The scale bar 10um.

After combining the glucose and lipid metabolism of each acinus, we constructed a metabolic "map" with axes representing ORR and lipid content (fig 5.2h). Each dot in the scatterplot is derived from measurements of one acinus on day 12 (~50-200 cells per acinus). As shown in the figure, PME, T47D and MDA-MB-231 cells were clearly distinguishable in the 2D scatterplot based on their metabolic signatures.

5.4 Discussion

We report that multiple metabolic changes at the single cell level can be visualized during normal acinus formation, tumor spheroid growth, and cancer cell proliferation using multi-modal NLOM. Using CRS and TPEF microscopy, we captured glucose and lipid metabolic differences between normal primary mammary epithelial cells and two different cancer cell lines. In addition, we observed the differential impact of hormonal stimulation on normal vs cancer cells grown in a 3D collagen-rich matrix. Making use of deuterium labeling of glucose, we observed a correlation between cancer cell metabolism and cancer invasiveness, which originated from the utilization of glucose-derived carbons in support of cellular biosynthesis.

Normal mammary epithelial cells exhibit three distinct metabolic phases during acinus formation, characterized by gradually increasing lipid accumulation and progressive redox state changes from glycolysis to oxidative phosphorylation (Fig. 1). Early in the process (days 1-4), cells have lower optical redox ratios and low lipid accumulation. At this stage, acini are composed of 1-8 cells each with significant cell-ECM contact but little cell-cell interaction. Interactions with the ECM and the low

activation of focal adhesion kinase (FAK) promotes cell cycle progression [38]. Under these conditions, cells start to prepare for proliferation by increasing biosynthesis of DNA, organelles, membranes, etc. To meet the high demand for biomass, glucose is utilized not only for providing energy but also as a source of carbon-based biomass. The metabolite of glucose, citrate, is converted to acetyl-CoA and used for lipid and nucleotide production [39]. The amount of lipid droplets stored in the cytoplasm is seen to decrease, either to fuel biological activities or to synthesize cell membranes. As the acini grow, cell-cell contact arrests/inhibits proliferation rates through the Hippo/YAP pathway [40]. At this time point, the cells no longer need large amounts of biomolecule synthesis and switch back to oxidative phosphorylation to more efficiently produce ATP. Due to the low usage of lipid, the lipid droplets reappear in the cytosol. This stage of the acinus growth process gives rise to an increase in the optical redox ratio and lipid content from day 4 to day 8, when the acini generally grow to a size of 18-24 cells. Finally, by day 10-12, both the ORR and lipid content are stabilized, indicating the formation of a mature acinus.

Interestingly, we observe spatial variations in metabolism in the polarized acinus around day 8. The ORR images reveal that apical cells in the center have a higher oxidative rate while the peripheral basal cells are more glycolytic. This is likely due to gradients that drive nutrient and signaling differences. Tissue polarity has been shown to be essential for mammary epithelial cells to form healthy alveolar structures and maintain normal breast function [41]. Only basal cells are directly exposed to signaling from the ECM, especially from the binding of β4 integrin and laminin I [42]. The cells in the center of the acinus have high cell contact inhibition and lack hemidesmosome formation

and NFκB activation which promotes cell apoptosis [43]. These cells exhibit increased ORR levels and disappear in 2-4 days, leaving a hollow center in the acinus. Indeed, the increase of ORR is a predictor for cell apoptosis [44]. The increase of ORR as a predictor for cell apoptosis has been reported [130]. Moreover, the availability of glucose and oxygen is location sensitive in polarized acini structures. The high polarity of exposure to nutrients and signaling has been shown to be essential for mammary epithelial cells to form healthy alveoli structures and maintain normal breast function [131]. All these observations were enabled by the high resolution of NLOM as two populations of PME cells with distinctive redox ratios and cell fate were identified.

Compared to normal epithelial breast cells, acini formed from cancer cells display altered morphologies. The T47D acinus has a solid core whereas acini grown from MDA-MB-231 cells feature irregular shapes. The appearance of cells in our 3D cultures strongly mimics observations from patient biopsies; normal breast tissue features tubular alveolar structures, ductal carcinoma in situ presents cell proliferation towards the lumen, and the cancer cells in invasive ductal carcinoma infiltrate into the stromal tissue [45]. We observe that each cell line examined here has distinctive NLOM-derived metabolic signatures. As predicted by the Warburg effect, T47D and MDA-MB-231 cancer cells are found to be more glycolytic compared to normal breast cells. The two malignant cancer cell lines are also characterized by significantly different optical redox ratios. Previous studies reported similar observations by monitoring glucose metabolism alone to separate distinct breast cancer subtypes [13, 23, 46, 47]. Our study expands on previous work by adding lipid content as an additional defining feature, motivated by recent work that suggests that abnormal lipid metabolism can be another hallmark for various cancers [48].

Cancer cells prefer de novo lipid synthesis and have been observed to upregulate fatty acid synthesis (FASN) enzyme expression. ERBB2, PI3K, ATP citrate lyase and various reported mutations in cancers are also known to affect lipid metabolism [20]. Thus, the combination of lipid content and ORR provides additional quantitative information that refines our ability to characterize cancer cell metabolism beyond what can be determined from each parameter separately.This is the first time that lipid content has been added as an additional defining feature. In fact, the lipid content in the three cell lines varies more dramatically (27-fold range) than the optical redox ratio (~1.2X). More and more researches pointed out that the abnormal lipid metabolism can be another hallmark for cancers [135].

Chapter 6

Cancer metastasis and their metabolic signatures

6.1 Introduction

Breast tissue is known to be a dynamic site of lipid metabolism[136] and LD abundance changes dramatically during development[137, 138], menstruation, pregnancy, and lactation[139]. LDs are formed by budding off the endoplasmic reticulum (ER) and store fatty acids (FAs) in the form of diacyl- and triacylglycerol (DAG and TAG, respectively) and cholesterol in the form of cholesteryl esters. LDs interact with a multitude of organelles (i.e. peroxisomes, autophagosomes, and mitochondria) to shuttle FAs for incorporation into cell membranes, post-translational modifications, and FAO[140]. In order for long chain FAs to enter any of these pathways they must first be activated to become acyl-CoAs. Long-chain (12-20 carbons) FAs are activated by typical acyl-CoA synthetase ligase (ACSL) enzyme family, including members 1, 3, 4, and 5[141]. Acyl-CoAs may enter FAO, which yields acetyl-CoAs utilized in the tricarboxylic acid cycle (TCA), generating nicotinamide adenine dinucleotide (NADH) utilized for oxidative phosphorylation (OxPhos) to ultimately produce adenosine triphosphate (ATP).

Dysregulated lipid metabolism and FAO have recently been linked to breast cancer progression. Photoacoustic imaging of the MMTV-PyMT-driven breast cancer

model demonstrated that transformation of normal breast tissue to invasive carcinoma resulted in a progressive decrease of cytoplasmic LD abundance[142]. In line with this, pharmacological activation of peroxisome proliferator-activated receptor γ (PPARγ) caused accumulation of LDs in breast cancer cells and decreased their proliferation[143]. Furthermore, Src[144] and Myc[145] oncogenes were recently reported to contribute to lipid metabolism dysregulation in TNBC. Src kinase has been reported to stimulate FAO in a positive feedback loop, and pharmacological and genetic inhibition of FAO blocked TNBC metastasis *in vivo*[144]. Myc has also been reported to stimulate FAO and pharmacological inhibition of FAO blocked tumor growth of Myc-driven TNBC tumors[145]. These data indicate that lipid metabolism represents a potential therapeutic target in TNBC.

6.2 Experiment details

We observed that tumor cells that had different levels of invasiveness presented different metabolic signatures. Thus, we tested whether the metabolic differences were due to different levels of cancer invasiveness. 17β-estradiol was known to increases the cancer invasiveness in ER+ breast cancers and affects the cancer response to chemotherapy [146]. However, the presence of E2 is crucial for normal organ development and functions including breast milk secretion [147, 148]. We added 17β-estradiol to both matured T47D (ER+ breast cancer cell lines) and PME (normal) acini at physiologically relevant concentrations (10-8 M) and monitored the acini morphological and metabolic responses after 3 days.

6.3 Results

We observed that tumor cells that had different levels of invasiveness presented different metabolic signatures. Thus, we tested whether the metabolic differences were due to different levels of cancer invasiveness. 17β-estradiol was known to increases the cancer invasiveness in ER+ breast cancers and affects the cancer response to chemotherapy [146]. However, the presence of E2 is crucial for normal organ development and functions including breast milk secretion [147, 148]. We added 17β-estradiol to both matured T47D (ER+ breast cancer cell lines) and PME (normal) acini at physiologically relevant concentrations (10-8 M) and monitored the acini morphological and metabolic responses after 3 days.

The PME cells did not show any morphology change with or without E2. However, the T47D breast cancer cells demonstrated higher numbers of broken acini ($p<0.01$) and a remodeling of the collagen fibers. In the control group (untreated with E2), 78% of the T47D cell clusters remained as spheroids which were wrapped with arbitrarily oriented collagen fibers (fig. 6.1a). However, 84% of the acini were no longer growth arrested and showed one or more extrusions of cancer cells after E2 treatment (fig. 6.1b). All the treated spheroids exhibited a visible remodeling of the ECM at the broken sites. Instead of organizing in a direction normal to the spheroid surface, the collagen fibers were highly polarized and aligned in the direction of extruded cancer cells, a structural feature that can benefit invasion [149].

Glucose and lipid metabolism were recorded for both PME and T47D cells treated with either DMSO (control) or E2 (fig 6.1c). The optical redox ratio of E2-treated PME cells decreased slightly from 0.34 to 0.32 (p=0.04), however the ORR of T47D cancer

cells dropped about 30% (p<0.01) when treated with E2. In contrast, lipid droplet content *increased* significantly in E2-treated PME cells (p=0.02) while the lipid content of T47D cells *diminished* by half (p=0.03). The effects of E2 on cell metabolism are shown in a metabolic scatter map and trends denoted with arrows (fig 6.1d). An increase in cancer invasiveness is observed to accompany metabolic adaptations to E2, wherein cancer cells become more glycolytic and have lower lipid content. Despite E2 stimulation, PME cells preserve acini structural integrity and demonstrate significant lipid accumulation that matches normal mammary epithelial cell function.

An increase in cancer invasiveness is observed to accompany metabolic adaptations to E2 wherein cancer cells become more glycolytic and have lower lipid content. Despite E2 stimulation, PME cells preserve acini structural integrity and demonstrate significant lipid accumulation that matches normal mammary epithelial cell function.

Our NLOM redox measurements are consistent with cancer cell Warburg metabolism and have been observed extensively in previous studies [7]. However, it is unclear from our lipid imaging results whether the inverse relationship between lipid accumulation and invasiveness is a consequence of impaired storage/synthesis or enhanced lipid utilization. In order to further explore these redox/lipid signatures, we used deuterium labeling and stimulated Raman scattering (SRS) microscopy to track carbon flow starting from glucose [123]. SRS microscopy probes different chemical vibrations by adjusting the optical frequency difference between two incident laser beams (pump and Stokes). In our experiment, we kept the optical frequency of the Stokes beam constant and tuned the optical frequency of the pump beam to image both natural

aliphatic lipids (Raman shift is 2850 cm-1) and deuterated hydro-carbons (Raman shift is 2175 cm-1).
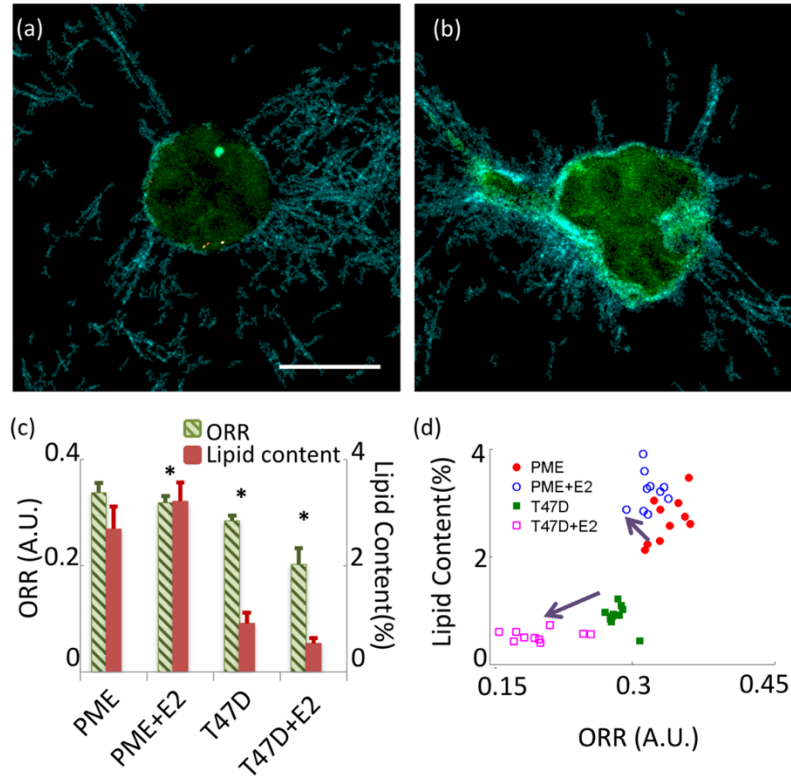
Figure 6.1. The morphological and metabolic changes with different cancer invasiveness. (a) the cross section of T47D acini before treated with E2; (b) the cross section of T47D acini after treated with E2. In both images, the NADH (green) is excited with TPEF, the collagen (blue) measured with SHG and the lipid droplets (red) are imaged with CARS. The scale bar is 10um. (c) The glucose and lipid metabolic response of T47D breast cancer cells and PME cells to E2. Both cell lines show statistically significantly different redox ratio and lipid content. (d) The combination of glucose and lipid metabolism of PME cells and T47D cells before and after adding E2. The solid circles and squares are the PME cells and T47D measurements before the adding the E2. The hollowed circles and squares are the cell metabolic measurements after treated with E2. Each single data points represent an average of all the cells in a whole acini structure. The purple arrows indicate the metabolic changing trend induced by adding E2.
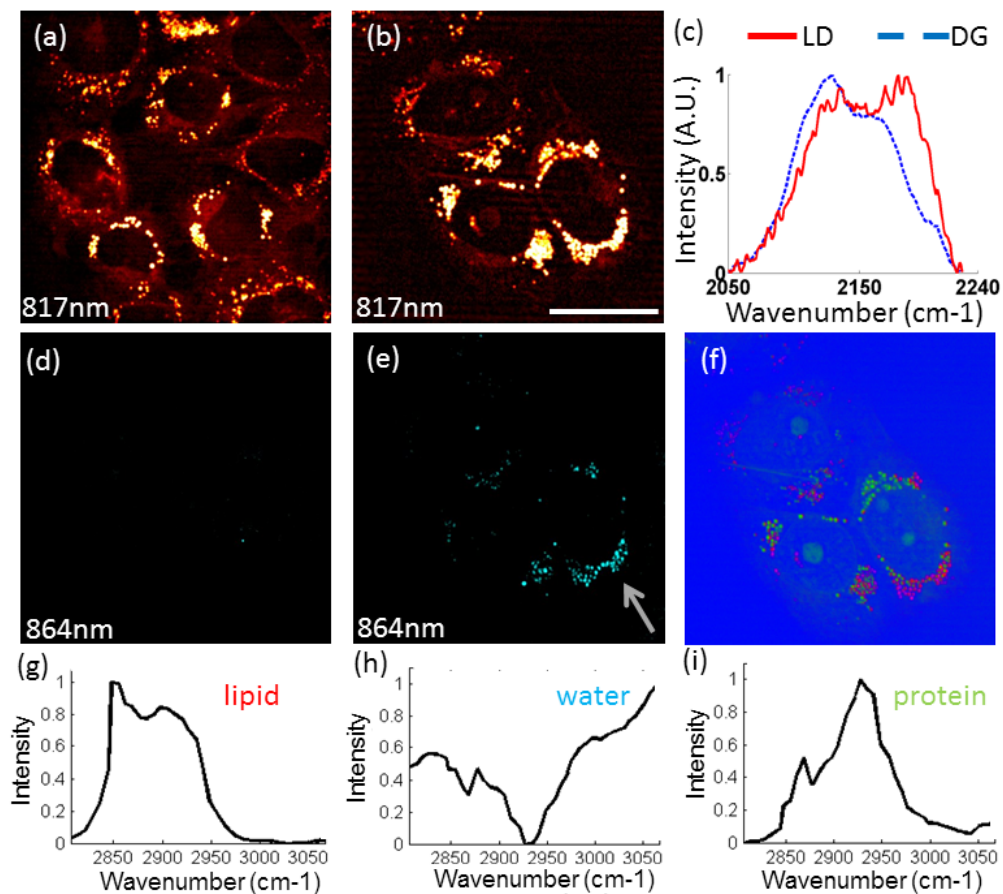
Figure 6.2. the SRS images of cells cultured in normal (a and b) and deuterated (d and e) glucose medium. (c) Normalized representative Raman spectrum of the pure deuterated glucose solution and the droplet structure pointed out by the arrow. The spectrum is acquired with confocal Raman microscopy and the data from 2000 cm^{-1} to 2250 cm^{-1} was normalized and shown here. (f) Pseudo color image of lipid (red), water (blue) and protein (green) for (e) based on vertex component analysis. (g) Representative spectrum of lipid that correspond to red pixels in (f). (h) Representative spectrum of water that correspond to blue pixels in (f). (i) Representative

We first tested the system sensitivity by imaging the T47D cancer cells cultured in normal and deuterated glucose medium. The SRS images of cells cultured under both conditions exhibited similar levels of normal lipid droplet formation (fig. 6.2.a and d) but only the cells cultured with deuterated glucose exhibited signals at the Raman shift of 2175 cm-1 (fig. 6.2.b and e). The Raman spectrum of droplets with deuterated material (pointed out by the arrow) was distinct from the Raman spectrum of deuterated glucose (fig. 6.2.c), underscoring that the hydrocarbon units originally derived from glucose were incorporated in newly synthesized and chemically distinct compounds in the droplets. We also collected hyperspectral SRS images in the 2800 cm-1 to 3050 cm-1 range and identified three major chemicals (lipid, water and protein) by vertex component analysis. The deuterated compounds were found to co-localize only with lipid droplets (red) (fig. 6.2.f) and confirmed the system capability to track the carbon flow in live cells for lipid synthesis.

PME, T47D and T47D breast cancer cells treated with E2 were cultured in 2D with deuterated glucose medium. After incubation for 12 hours, we measured the ORR, normal lipid droplet fraction (LD), and deuterated lipid droplet fraction (dLD) in the three groups (fig. 6.3). The amount of glucose-derived lipid was evaluated with the ratios of dLD/LD. Figure 4 a-c shows representative SRS images of normal lipid distribution for each group. The glucose-derived lipid droplets were visualized in the deuterium region (fig. 6.3d-f). Moreover, we observed newly synthesized lipid deposited at the outside of existing lipid droplets which formed donut-shaped dLDs (fig. 6.3f inset). PME cells exhibited ~3-fold greater levels of normal lipid accumulation compared with T47D cells

(p<0.01). The normal lipid content further decreased by 58% in the T47D cells treated with E2. However, T47D cells had elevated levels of deuterated lipids and the dLD/LD ratios were 5 times higher compared with PME cells (fig. 6.3 d and e). ER activated cancer cells exhibited stronger deuterated lipid signal intensities and the average dLD/LD ratio was 1.4 times higher (p=0.03), indicating increased lipid synthesis rates (fig.6.3 e and f).

To probe the lipid utilization rate with and without ER activation, we performed a pulse-chase experiment. T47D cells were first exposed to deuterated glucose medium for ~12 hours before switching to normal glucose medium. The SRS images of normal cellular lipid content and deuterated lipids were acquired at different time points to determine the average intensity ratios of dLD/LD. Figure 6.3.i-j shows representative images of deuterated signals measured at T = 0h, 6h and 12h. The deuterated signals exhibited exponential decays among which the E2 treatment increased lipid turnover rate by 3 hours (fig. 6.3.l). The lipid decay rate in cancer cells treated with E2 was 68% faster than in cells treated with DMSO, corresponding to a lipid turnover rate that is shorter by ~3 hours. The dLD/LD ratios of the two groups were log-transformed and the decay rates tested with one-way analysis of covariance revealing significant differences (p=0.04).
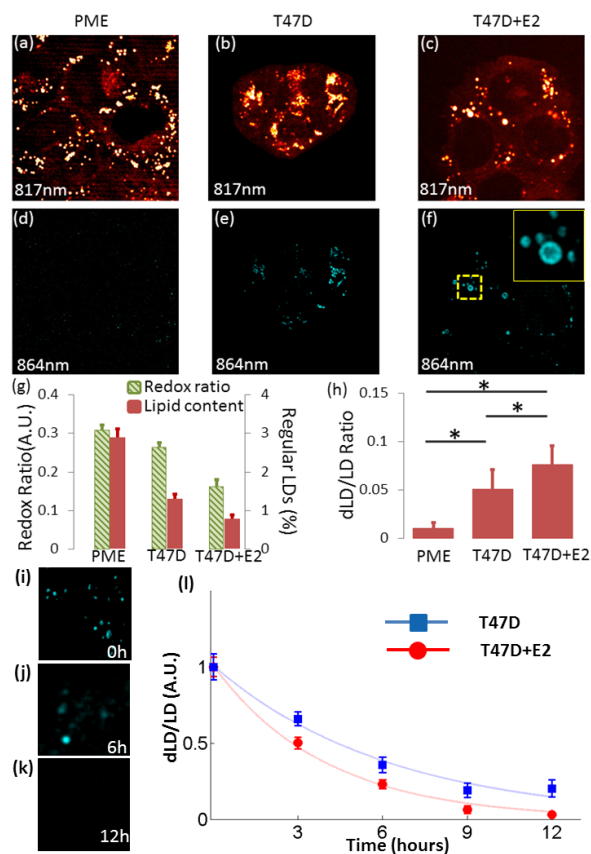
Figure 6.3. SRS images of normal lipid accumulation from (a) PME cells, (b) T47D cells and (c) T47D cells treated with estradiol. (d) The SRS images of deuterated lipid accumulation from PME cells, (e) T47D cells and (f) T47D cells treated with estradiol. Inset of image: zoom-in image of marked area showing the donut-shaped dLD as an indicator for newly synthesized LD. (g) The redox ratio and normal lipid accumulation between PME cells, T47D cells and T47D cells treated with estradiol. The error bars represent the standard deviation from 25 measurements. (h) the average intensity ratios of deuterated lipid and normal lipid from PME cells, T47D cells and T47D cells treated with estradiol. (i-k) representative images of deuterated lipids at T=0h, 6h, and 12h. (l) The dLD/LD decay for T47D cells treated with DMSO (blue square) and 17β-estradiol (red circle) over 24 hours. The data points represent deuterated signals were measured at time T=0h, 3h, 6h, 9h, and 12h. The solid lines represent exponential decay fitting of the data, dLD/LD=exp(-kt), where k corresponds to the rate at which the lipid signal disappears. The lipid decay rate in cancer cells treated with E2 was k=0.26 ± 0.02 *vs* cells treated with DMSO k=0.18 ± 0.01. At each time point, the deuterated signal and normal lipid signal are manually measured from 50 different lipid droplets in 25 cells on average. The error bars represent the standard deviation from 50 LDs.

ORR measurements were consistent with results obtained from our measurements of 3D acini. PME cells have ~20% higher optical redox ratios (greater oxidative phosphorylation) compared to the more glycolytic T47D cancer cells and the ORR further decreased by 28% (p<0.01) in T47D cells treated with E2 (fig. 6.3g). Furthermore, the higher the ORR, the lower the dLD/LD. Thus, the increased glycolytic rate is positively correlated with *de novo* lipid synthesis. When exogenously stimulated with E2, cancer cells adapted with increased aerobic glycolysis to benefit biosynthesis. Normal cells, in contrast, mainly relied on fatty acid uptake from the environment rather than the *de novo* lipid synthesis observed in cancer cells.

6.4 Discussion

Metabolic and ECM changes in response to 17β-estradiol (E2) stimulation further reveal key differences between normal and breast cancer cells. The disruptions of T47D spheroid structures and remodeled collagen polarization upon treatment of E2 have been linked to increased cancer invasiveness both in vitro and in vivo [150, 151]. Additionally, the T47D cancer cells became more glycolytic and demonstrated decreased level of lipid content. We know that a change in cancer invasiveness began by turning on/off multiple gene expressions which affected the metastatic potential and cell proliferation rate. Thus, the downstream of these alterations in cancer cell phenotypes took effect through adaptations in cellular metabolism which provided energy and biomass support. We observe that T47D cancer cells grow more glycolytic and display a decreased level of lipid content after E2 treatment. Our observation matches Ostrander et al's experiments

that the expression and blocking of the estrogen receptor in ER+ cancer cells decreases the redox ratio, a metric that may serve as a biomarker for cancer invasiveness.[71]. However, the ORR alone is insufficient for separating breast cancer from normal epithelial cells since both cell lines become more glycolytic in response to E2 treatment. Only by considering lipid storage of the two cell lines as an additional differentiator could the two populations be seen moving in different directions on the 2D-metabolic map (figure 3d). Our observations support the notion that with increased glycolysis, more glucose is used for de novo fatty acid synthesis in both cancer and normal cell line [152]. Nonetheless, whereas the PME cells preserve the lipid and prepare for milk secretion, cancer cells utilize lipids to prepare for cell proliferation (i.e. producing cell membrane) [153]. This is consistent with previous magnetic resonance spectroscopy studies showing that a decrease in neutral lipid accumulation in the cytoplasm is correlated with increased cell proliferation and malignancy [54, 55]. The results, again, demonstrated the importance to include lipid into metabolic analysis. Thus, the cancer invasiveness is strongly related to cell metabolism.

The correlation between lipid metabolism and cancer invasiveness is further explored in CRS imaging studies in which deuterated glucose is used to track carbon flow. Low deuterium signals in PME cell lipid droplets and higher dLD/LD values in T47D cells imply that cancer cells actively utilize deuterium-labeled carbons from glucose for de novo lipid synthesis. These results are in agreement with previous studies showing that normal cells preferentially take up circulating fatty acids while >90% of lipid in cancer cells is synthesized from glucose and intermediate products of glycolysis [154].

While untreated T47D breast cancer cells show moderate levels of dLD/LD and an intermediate optical redox ratio, E2-treated T47D cells display the highest dLD/LD, lowest ORR, and lowest unlabeled lipid droplet accumulation. Furthermore, in our pulse-chase study, the rate of disappearance of deuterated lipid following unlabeled glucose exposure is significantly higher for E2-treated cells (k=0.26 ± 0.02) *vs* cells treated with DMSO (k=0.18 ± 0.01). We conclude that cancer cells treated with E2 have increased lipid synthesis rates (elevated dLD/LD), faster lipid utilization rates (k = 0.26 ± 0.02), and higher glycolytic activity (lower ORR) compared to PME and untreated T47D cells. The decrease in neutral lipid accumulation in the cytoplasm has been correlated with increased cell proliferation and malignancy by magnetic resonance spectroscopy [155, 156]. Moreover, T47D cancer cells treated with E2 had higher dLD/LD ratios than untreated cells indicating an increase of lipid synthesis rate. The neutral lipid accumulation in cytoplasm reflected the joint effect of lipid synthesis rate and lipid utilization. To achieve a decrease in neutral lipid accumulation with increased lipid synthesis rate, the lipid utilization rate had to increase as well. Thus, the cancer cells increased both lipid synthesis and utilization rate to meet the demand for biomass and energy. The pulse chase experiment double proved the dynamics of the lipid metabolism. The exponential decay reflected the combined effect of lipid utilization of deuterated lipids and newly synthesized normal lipids. With E2 activation, the cancer cells presented faster decay compared with control group originated from an increase of lipid consumption.

More interestingly, the redox ratios decreased as the dLD/LD ratios increased. PME cells had highest redox ratio (high oxidative phosphorylation) but negligible

deuterated lipid, T47D breast cancer cells treated with E2 had lowest redox ratio (highest

glycolytic rate) but highest levels of deuterated lipids and T47D breast cancer cells

demonstrated moderate level of dLD/LD and a redox ratio in between. These

observations supported the backbone of Warburg effect that the aerobic glycolysis is

beneficial for glucose-based synthesis of biomolecules necessary for supporting cancer

cell proliferation. More than 93% of lipid supply in cancer cells came from the

intermediate product of glycolysis which was fully oxidized in normal cells [157]. Thus,

the changes of glucose and lipid metabolism were correlated and both would adapt to a

change of cancer invasiveness. In our cases, an increase in cancer invasiveness leaded to

increased proliferation rate which required doubling of cell membrane, proteins and DNA.

To meet the high demand of for biomass and energy, the cells adapted in two ways. On

one hand, the cancer cells became more glycolytic to provide carbon sources for

biosynthesis. On the other hand, they increased the utilization rate of lipid storage to get

materials for either beta oxidation or building blocks for cell organelles. The level of the

metabolic adaptation is determined by the need which is correlated with cancer

invasiveness. Thus, the abnormal metabolic activity (Warburg effect) is more than a

biomarker to differentiate cancer and normal cancer cells but an indicator for cancer

metastatic stages.

6.5 Concluding remarks

In conclusion, the combining of glucose and lipid metabolism can better characterize

cancer cell behaviors. By combining of glucose and lipid metabolism, we quantified the

biomass synthesis rate and utilization rate together and identified a correlation of

increased lipid synthesizing and utilization rate with cancer invasiveness. The combining

of the two can greatly advance our knowledge about the mechanism of the cancer

metastasis, their drug response and, potentially, to be used for developing personalized

treatment.

Chapter 7

Conclusion

Cancer has a long history and was first described around 1600 B.C.; however, the mechanism of cancer development and an efficient treatment remains elusive. Right now, it affects about 7.6 million people every year around the world and only one third of them can survive the disease. Despite the development of modern technology, the most popular treatment regime remains the same, chemotherapy, radiotherapy and surgery. First, the doctors design the treatment by mixing different chemotherapy drugs based on the histological information extracted from the biopsy. The working mechanism is to either target cancer cells' surface biomarkers or simply just all fast proliferating cells. The patients would either take the drug before the surgery (neoadjuvant chemotherapy) or after (adjuvant chemotherapy). However, 30% of the patients will not benefit from it but still have to suffer from the side effects.

Instead of looking for different types of biomarkers for different types of cancer, abnormal metabolism is a common feature that shares by all cancer types. The most famous observation on cancer metabolism would be the "Warburg effect", which describes the aerobic glycolysis in cancer cells. The main idea behind the concept is that cancer cells prefer glycolysis to better fuel their fast proliferation. The intermediate

products of glycolysis serves as precursors for *de novo* biosynthesis of nucleotides, amino acid and fatty acid which are the basic building blocks for cells. Since the finding of such phenomenon, numerous studies are conducted to search for potential applications on cancer diagnosis and treatment. However, stem cells, endothelial cells and insulin-activated cells all present Warburg-effect-similar metabolic signatures. The biological system of our body is too complicated to be described with just parameter. Moreover, to be able to observe metabolic changes in live cells with high spatial and temporal resolution would greatly benefit researches.

In our work, label-free non-linear optical microscopy (NLOM) methods based on two-photon excited fluorescence (TPEF) have been used to form high-resolution images of redox state in cells and tissues based on intrinsic NADH and FAD+ fluorescence. We demonstrate that label-free NLOM measurements of TPEF-derived redox state (optical redox ratio, ORR = FAD+/(NADH + FAD+)) can give comparable measurements to conventional flux analyzer. Both measurements have a linear correlation under a range of oxygen consumption conditions relevant for cancer imaging. Moreover, we combined ORR with coherent Raman imaging of lipid formation and second harmonic generation of extracellular matrix (ECM) collagen to quantitatively characterize cancer cells and their relative invasive potential. In addition, we confirm, using coherent Raman and deuterium labeling methods, that glucose is a significant source for the cellular synthesis of lipid in glycolytic breast cancer cells. Live cell metabolism was imaged in 3D models of primary mammary epithelial cells (PME) and 2 cancer cell lines, T47D and MDA-MB-231. The combination of ORR and lipid volume fraction was unique for each line. Upon treating cells with 17β-estradiol (E2), both normal (PME) cells and ER-positive

breast cancer cells (T47D) exhibited an increased glycolysis rate with significant

reorganization of ECM collagen in 3D T47D models. Importantly, PME cells displayed

increased lipid content while the lipid storage in cancer cells decreased ($p<0.001$) with E2

stimulation. Furthermore, we observed an increase in both lipid synthesis and

consumption rates in E2-treated T47D cancer cells cultured in deuterated glucose by

tracking the formation and disappearance of deuterated lipids. These results suggest that

the combination of multiple NLOM imaging endpoints, including ORR, lipid content,

and SHG, can be used to characterize and understand key metabolic features that are

hallmarks of disease.

To our knowledge, it is the first time the glucose metabolism and lipid

metabolism are combined to characterize cancer cells. The two processes describe both

the catabolism and anabolism in cancer metabolism and can separate the cell

subpopulations that cannot if merely rely on glucose metabolism. Furthermore, the

dynamic metabolic changes we observed illustrated the potential of label-free nonlinear

optical imaging microscopy. Complex physiological processes can be directly visualized

without the interference of exogenous chemicals. The high spatial and temporal

resolution makes the technology an idea tool to study cancer heterogeneity with

metabolic responses happening from seconds to weeks. The non-invasive nature and 3D

sectioning effect would even allow *in vivo* studies on patient or animal models

conveniently.

Reference

1. Sokoloff, L., et al., *The [14C]deoxyglucose method for the measurement of local cerebral glucose utilization: theory, procedure, and normal values in the conscious and anesthetized albino rat.* J Neurochem, 1977. **28**(5): p. 897-916.
2. Belanger, M., I. Allaman, and P.J. Magistretti, *Brain energy metabolism: focus on astrocyte-neuron metabolic cooperation.* Cell Metab, 2011. **14**(6): p. 724-38.
3. Denning, C., et al., *Cardiomyocytes from human pluripotent stem cells: From laboratory curiosity to industrial biomedical platform.* Biochim Biophys Acta, 2016. **1863**(7 Pt B): p. 1728-48.
4. Sakurai, Y., M. Ochiai, and T. Funabiki, *Assessment of in vivo glucose kinetics using stable isotope tracers to determine their alteration in humans during critical illness.* Surg Today, 2000. **30**(1): p. 1-10.
5. Lenzen, S., *A fresh view of glycolysis and glucokinase regulation: history and current status.* J Biol Chem, 2014. **289**(18): p. 12189-94.
6. Alba-Lois, L. and C. Segal-Kischinevzky, *Beer & Wine Makers.* Nature, 2010.
7. Lunt, S.Y. and M.G. Vander Heiden, *Aerobic glycolysis: meeting the metabolic requirements of cell proliferation.* Annu Rev Cell Dev Biol, 2011. **27**: p. 441-64.
8. Chambers, D.A., D.W. Martin, Jr., and Y. Weinstein, *The effect of cyclic nucleotides on purine biosynthesis and the induction of PRPP synthetase during lymphocyte activation.* Cell, 1974. **3**(4): p. 375-80.
9. Warburg, O., *On the origin of cancer cells.* Science, 1956. **123**(3191): p. 309-14.
10. Manning, B.D. and L.C. Cantley, *AKT/PKB signaling: navigating downstream.* Cell, 2007. **129**(7): p. 1261-74.
11. Matoba, S., et al., *p53 regulates mitochondrial respiration.* Science, 2006. **312**(5780): p. 1650-3.
12. Newsholme, E.A., B. Crabtree, and M.S. Ardawi, *The role of high rates of glycolysis and glutamine utilization in rapidly dividing cells.* Biosci Rep, 1985. **5**(5): p. 393-400.
13. Clemens, M.J., *Targets and mechanisms for the regulation of translation in malignant transformation.* Oncogene, 2004. **23**(18): p. 3180-8.
14. Vander Heiden, M.G., L.C. Cantley, and C.B. Thompson, *Understanding the Warburg effect: the metabolic requirements of cell proliferation.* Science, 2009. **324**(5930): p. 1029-33.
15. Braccini, L., et al., *PI3K keeps the balance between metabolism and cancer.* Adv Biol Regul, 2012. **52**(3): p. 389-405.
16. LeBleu, V.S., et al., *PGC-1alpha mediates mitochondrial biogenesis and oxidative phosphorylation in cancer cells to promote metastasis.* Nat Cell Biol, 2014. **16**(10): p. 992-1003, 1-15.
17. Kuhajda, F.P., *Fatty-acid synthase and human cancer: new perspectives on its role in tumor biology.* Nutrition, 2000. **16**(3): p. 202-8.
18. Kuhajda, F.P., *Fatty acid synthase and cancer: new application of an old pathway.* Cancer Res, 2006. **66**(12): p. 5977-80.
19. Steinhauser, M.L., et al., *Multi-isotope imaging mass spectrometry quantifies stem cell division and metabolism.* Nature, 2012. **481**(7382): p. 516-9.
20. Lewis, D.Y., D. Soloviev, and K.M. Brindle, *Imaging tumor metabolism using positron emission tomography.* Cancer J, 2015. **21**(2): p. 129-36.

21.   Matsuo, M., et al., *Magnetic resonance imaging of the tumor microenvironment in radiotherapy: perfusion, hypoxia, and metabolism.* Semin Radiat Oncol, 2014. **24**(3): p. 210-7.

22.   Larson, P.E., et al., *Investigation of tumor hyperpolarized [1-13C]-pyruvate dynamics using time-resolved multiband RF excitation echo-planar MRSI.* Magn Reson Med, 2010. **63**(3): p. 582-91.

23.   Frey, A.J., et al., *LC-quadrupole/Orbitrap high-resolution mass spectrometry enables stable isotope-resolved simultaneous quantification and C-isotopic labeling of acyl-coenzyme A thioesters.* Anal Bioanal Chem, 2016.

24.   Bernsen, M.R., et al., *Biomarkers in preclinical cancer imaging.* Eur J Nucl Med Mol Imaging, 2015. **42**(4): p. 579-96.

25.   Munoz-Pinedo, C., N. El Mjiyad, and J.E. Ricci, *Cancer metabolism: current perspectives and future directions.* Cell Death Dis, 2012. **3**: p. e248.

26.   Danilo, C. and P.G. Frank, *Cholesterol and breast cancer development.* Curr Opin Pharmacol, 2012. **12**(6): p. 677-82.

27.   Sebastian, C., *Tracking down the origin of cancer: metabolic reprogramming as a driver of stemness and tumorigenesis.* Crit Rev Oncog, 2014. **19**(5): p. 363-82.

28.   Kukreti, S., et al., *Intrinsic tumor biomarkers revealed by novel double-differential spectroscopic analysis of near-infrared spectra.* J Biomed Opt, 2007. **12**(2): p. 020509.

29.   Walsh, A.J., et al., *Optical metabolic imaging identifies glycolytic levels, subtypes, and early-treatment response in breast cancer.* Cancer Res, 2013. **73**(20): p. 6164-74.

30.   Cerussi, A.E., et al., *Diffuse optical spectroscopic imaging correlates with final pathological response in breast cancer neoadjuvant chemotherapy.* Philos Trans A Math Phys Eng Sci, 2011. **369**(1955): p. 4512-30.

31.   Meric-Bernstam, F. and A.M. Gonzalez-Angulo, *Targeting the mTOR signaling network for cancer therapy.* J Clin Oncol, 2009. **27**(13): p. 2278-87.

32.   Ansell, S.M., et al., *Low-dose, single-agent temsirolimus for relapsed mantle cell lymphoma: a phase 2 trial in the North Central Cancer Treatment Group.* Cancer, 2008. **113**(3): p. 508-14.

33.   Chan, S., et al., *Phase II study of temsirolimus (CCI-779), a novel inhibitor of mTOR, in heavily pretreated patients with locally advanced or metastatic breast cancer.* J Clin Oncol, 2005. **23**(23): p. 5314-22.

34.   Motzer, R.J., et al., *Efficacy of everolimus in advanced renal cell carcinoma: a double-blind, randomised, placebo-controlled phase III trial.* Lancet, 2008. **372**(9637): p. 449-56.

35.   Margolin, K., et al., *CCI-779 in metastatic melanoma: a phase II trial of the California Cancer Consortium.* Cancer, 2005. **104**(5): p. 1045-8.

36.   Hudes, G., et al., *Temsirolimus, interferon alfa, or both for advanced renal-cell carcinoma.* N Engl J Med, 2007. **356**(22): p. 2271-81.

37.   Mondesire, W.H., et al., *Targeting mammalian target of rapamycin synergistically enhances chemotherapy-induced cytotoxicity in breast cancer cells.* Clin Cancer Res, 2004. **10**(20): p. 7031-42.

38.   Beuvink, I., et al., *The mTOR inhibitor RAD001 sensitizes tumor cells to DNA-damaged induced apoptosis through inhibition of p21 translation.* Cell, 2005. **120**(6): p. 747-59.

39.   Yap, T.A., et al., *Drugging PI3K in cancer: refining targets and therapeutic strategies.* Curr Opin Pharmacol, 2015. **23**: p. 98-107.

40.   Dillon, L.M. and T.W. Miller, *Therapeutic targeting of cancers with loss of PTEN function.* Curr Drug Targets, 2014. **15**(1): p. 65-79.

41.   Sun, Y., H. Tian, and L. Wang, *Effects of PTEN on the proliferation and apoptosis of colorectal cancer cells via the phosphoinositol-3-kinase/Akt pathway.* Oncol Rep, 2015. **33**(4): p. 1828-36.

42. Miller, T.W., et al., *Loss of Phosphatase and Tensin homologue deleted on chromosome 10 engages ErbB3 and insulin-like growth factor-I receptor signaling to promote antiestrogen resistance in breast cancer.* Cancer Res, 2009. **69**(10): p. 4192-201.

43. Hopkins, B.D., et al., *A secreted PTEN phosphatase that enters cells to alter signaling and survival.* Science, 2013. **341**(6144): p. 399-402.

44. Kim, S.M., et al., *Targeting cancer metabolism by simultaneously disrupting parallel nutrient access pathways.* J Clin Invest, 2016. **126**(11): p. 4088-4102.

45. Kridel, S.J., et al., *Orlistat is a novel inhibitor of fatty acid synthase with antitumor activity.* Cancer Res, 2004. **64**(6): p. 2070-5.

46. Flavin, R., et al., *Fatty acid synthase as a potential therapeutic target in cancer.* Future Oncol, 2010. **6**(4): p. 551-62.

47. Orita, H., et al., *Selective inhibition of fatty acid synthase for lung cancer treatment.* Clin Cancer Res, 2007. **13**(23): p. 7139-45.

48. Sabnis, H.S., R.R. Somasagara, and K.D. Bunting, *Targeting MYC Dependence by Metabolic Inhibitors in Cancer.* Genes (Basel), 2017. **8**(4).

49. Ross, S.J. and S.E. Critchlow, *Emerging approaches to target tumor metabolism.* Curr Opin Pharmacol, 2014. **17**: p. 22-9.

50. Elf, S.E. and J. Chen, *Targeting glucose metabolism in patients with cancer.* Cancer, 2014. **120**(6): p. 774-80.

51. Guo, D., et al., *Targeting SREBP-1-driven lipid metabolism to treat cancer.* Curr Pharm Des, 2014. **20**(15): p. 2619-26.

52. Kobat, D., et al., *Deep tissue multiphoton microscopy using longer wavelength excitation.* Opt Express, 2009. **17**(16): p. 13354-64.

53. Cox, G., *Biological applications of second harmonic imaging.* Biophys Rev, 2011. **3**(3): p. 131.

54. Springer, S., et al., *Examination of wound healing after curettage by multiphoton tomography of human skin in vivo.* Skin Res Technol, 2017.

55. Zeitoune, A.A., et al., *Epithelial Ovarian Cancer Diagnosis of Second-Harmonic Generation Images: A Semiautomatic Collagen Fibers Quantification Protocol.* Cancer Inform, 2017. **16**: p. 1176935117690162.

56. Tilbury, K.B., et al., *Stromal alterations in ovarian cancers via wavelength dependent Second Harmonic Generation microscopy and optical scattering.* BMC Cancer, 2017. **17**(1): p. 102.

57. Balu, M., et al., *Rapid mesoscale multiphoton microscopy of human skin.* Biomed Opt Express, 2016. **7**(11): p. 4375-4387.

58. Chuang, S.C., et al., *Circulating biomarkers of tryptophan and the kynurenine pathway and lung cancer risk.* Cancer Epidemiol Biomarkers Prev, 2014. **23**(3): p. 461-8.

59. Bosnyak, E., et al., *Imaging cerebral tryptophan metabolism in brain tumor-associated depression.* EJNMMI Res, 2015. **5**(1): p. 56.

60. Sordillo, L.A., et al., *Differences in fluorescence profiles from breast cancer tissues due to changes in relative tryptophan content via energy transfer: tryptophan content correlates with histologic grade and tumor size but not with lymph node metastases.* J Biomed Opt, 2014. **19**(12): p. 125002.

61. Sordillo, L.A., et al., *Optical spectral fingerprints of tissues from patients with different breast cancer histologies using a novel fluorescence spectroscopic device.* Technol Cancer Res Treat, 2013. **12**(5): p. 455-61.

62. Eichhorn, R., et al., *Early diagnosis of melanotic melanoma based on laser-induced melanin fluorescence.* J Biomed Opt, 2009. **14**(3): p. 034033.

63. Krasieva, T.B., et al., *Two-photon excited fluorescence lifetime imaging and spectroscopy of melanins in vitro and in vivo.* J Biomed Opt, 2013. **18**(3): p. 31107.

64.   Balu, M., et al., *Distinguishing between benign and malignant melanocytic nevi by in vivo multiphoton microscopy.* Cancer Res, 2014. **74**(10): p. 2688-97.

65.   Tilbury, K. and P.J. Campagnola, *Applications of second-harmonic generation imaging microscopy in ovarian and breast cancer.* Perspect Medicin Chem, 2015. **7**: p. 21-32.

66.   Keikhosravi, A., et al., *Second-harmonic generation imaging of cancer.* Methods Cell Biol, 2014. **123**: p. 531-46.

67.   Zipfel, W.R., R.M. Williams, and W.W. Webb, *Nonlinear magic: multiphoton microscopy in the biosciences.* Nat Biotechnol, 2003. **21**(11): p. 1369-77.

68.   Chance, B., et al., *Oxidation-reduction ratio studies of mitochondria in freeze-trapped samples. NADH and flavoprotein fluorescence signals.* J Biol Chem, 1979. **254**(11): p. 4764-71.

69.   Walsh, A.J., et al., *Quantitative optical imaging of primary tumor organoid metabolism predicts drug response in breast cancer.* Cancer Res, 2014. **74**(18): p. 5184-94.

70.   Barhoumi, R., et al., *Multiphoton spectral analysis of benzo[a]pyrene uptake and metabolism in breast epithelial cell lines.* J Toxicol Sci, 2009. **34**(1): p. 13-25.

71.   Ostrander, J.H., et al., *Optical redox ratio differentiates breast cancer cell lines based on estrogen receptor status.* Cancer Res, 2010. **70**(11): p. 4759-66.

72.   Varone, A., et al., *Endogenous two-photon fluorescence imaging elucidates metabolic changes related to enhanced glycolysis and glutamine consumption in precancerous epithelial tissues.* Cancer Res, 2014. **74**(11): p. 3067-75.

73.   Xu, H.N., et al., *Quantitative mitochondrial redox imaging of breast cancer metastatic potential.* J Biomed Opt, 2010. **15**(3): p. 036010.

74.   Chance, B., R.W. Estabrook, and A. Ghosh, *Damped Sinusoidal Oscillations of Cytoplasmic Reduced Pyridine Nucleotide in Yeast Cells.* Proc Natl Acad Sci U S A, 1964. **51**: p. 1244-51.

75.   Veech, R.L., *The determination of the redox states and phosphorylation potential in living tissues and their relationship to metabolic control of disease phenotypes.* Biochem Mol Biol Educ, 2006. **34**(3): p. 168-79.

76.   Ji, J., et al., *Mitochondria-related miR-141-3p contributes to mitochondrial dysfunction in HFD-induced obesity by inhibiting PTEN.* Sci Rep, 2015. **5**: p. 16262.

77.   Chiara Stringari, R.A.E., Kira T. Pate, Marian L. Waterman, Peter J. Donovan, and Enrico Gratton, *Metabolic trajectory of cellular differentiation in small intestine by Phasor Fluorescence Lifetime Microscopy of NADH.* Scientific Reports, 2012. **2**: p. 9.

78.   Skala, M. and N. Ramanujam, *Multiphoton redox ratio imaging for metabolic monitoring in vivo.* Methods Mol Biol, 2010. **594**: p. 155-62.

79.   Raman, C.V. and K.S. Krishnan, *A new type of secondary radiation.* Nature, 1928. **121**: p. 501-502.

80.   Haka, A.S., et al., *In vivo margin assessment during partial mastectomy breast surgery using raman spectroscopy.* Cancer Res, 2006. **66**(6): p. 3317-22.

81.   Wang, W., et al., *Real-time in vivo cancer diagnosis using Raman spectroscopy.* J Biophotonics, 2015. **8**(7): p. 527-45.

82.   van der Geer, S., et al., *The incidence of skin cancer in dermatology.* Clin Exp Dermatol, 2013. **38**(7): p. 724-9.

83.   Teh, S.K., et al., *Diagnostic potential of near-infrared Raman spectroscopy in the stomach: differentiating dysplasia from normal tissue.* Br J Cancer, 2008. **98**(2): p. 457-65.

84.   Molckovsky, A., et al., *Diagnostic potential of near-infrared Raman spectroscopy in the colon: differentiating adenomatous from hyperplastic polyps.* Gastrointest Endosc, 2003. **57**(3): p. 396-402.

85.   Bergholt, M.S., et al., *In vivo, real-time, transnasal, image-guided Raman endoscopy: defining spectral properties in the nasopharynx and larynx.* J Biomed Opt, 2012. **17**(7): p. 077002.

86.   Feng, S., et al., *Surface-enhanced Raman spectroscopy of saliva proteins for the noninvasive differentiation of benign and malignant breast tumors.* Int J Nanomedicine, 2015. **10**: p. 537-47.

87.   Chung, C.Y. and E.O. Potma, *Biomolecular imaging with coherent nonlinear vibrational microscopy.* Annu Rev Phys Chem, 2013. **64**: p. 77-99.

88.   Terhune, R.W., P.D. Maker, and C.M. Savage, *Measurements of Nonlinear Light Scattering.* Physical Review Letters, 1965. **14**(17): p. 681-&.

89.   Freudiger, C.W., et al., *Stimulated Raman Scattering Microscopy with a Robust Fibre Laser Source.* Nat Photonics, 2014. **8**(2): p. 153-159.

90.   Wang, Z., W. Zheng, and Z. Huang, *Lock-in-detection-free line-scan stimulated Raman scattering microscopy for near video-rate Raman imaging.* Opt Lett, 2016. **41**(17): p. 3960-3.

91.   Lu, F.K., et al., *Multicolor stimulated Raman scattering (SRS) microscopy.* Mol Phys, 2012. **110**(15-16): p. 1927-1932.

92.   Freudiger, C.W., et al., *Highly specific label-free molecular imaging with spectrally tailored excitation stimulated Raman scattering (STE-SRS) microscopy.* Nat Photonics, 2011. **5**(2): p. 103-109.

93.   Nascimento, J.M.P. and J.M.B. Dias, *Vertex component analysis: A fast algorithm to unmix hyperspectral data.* Ieee Transactions on Geoscience and Remote Sensing, 2005. **43**(4): p. 898-910.

94.   Beatty, K.E., et al., *Fluorescence visualization of newly synthesized proteins in mammalian cells.* Angew Chem Int Ed Engl, 2006. **45**(44): p. 7364-7.

95.   Chozinski, T.J., et al., *Expansion microscopy with conventional antibodies and fluorescent proteins.* Nat Methods, 2016. **13**(6): p. 485-8.

96.   Freudiger, C.W., et al., *Label-free biomedical imaging with high sensitivity by stimulated Raman scattering microscopy.* Science, 2008. **322**(5909): p. 1857-61.

97.   Ji, M., et al., *Detection of human brain tumor infiltration with quantitative stimulated Raman scattering microscopy.* Sci Transl Med, 2015. **7**(309): p. 309ra163.

98.   Wei, L., et al., *Imaging complex protein metabolism in live organisms by stimulated Raman scattering microscopy with isotope labeling.* ACS Chem Biol, 2015. **10**(3): p. 901-8.

99.   Jeffrey L. Suhalim, C.-Y.C., Magnus B. Lilledahl, Ryan S. Lim, Moshe Levi,k Bruce J. Tromberg, and Eric O. Potma, *Characterization of Cholesterol Crystals in Atherosclerotic Plaques Using Stimulated Raman Scattering and Second-Harmonic Generation Microscopy.* Biophysical Journal, 2012. **102**: p. 1988-1995.

100.   Tabarangao, J.T. and A.D. Slepkov, *Mimicking Multimodal Contrast with Vertex Component Analysis of Hyperspectral CARS Images.* Journal of Spectroscopy, 2015: p. 1-8.

101.   Rice, W.L., D.L. Kaplan, and I. Georgakoudi, *Two-photon microscopy for non-invasive, quantitative monitoring of stem cell differentiation.* PLoS One, 2010. **5**(4): p. e10075.

102.   Scholz, R., et al., *Flavin and pyridine nucleotide oxidation-reduction changes in perfused rat liver. I. Anoxia and subcellular localization of fluorescent flavoproteins.* J Biol Chem, 1969. **244**(9): p. 2317-24.

103.   Rocheleau, J.V., W.S. Head, and D.W. Piston, *Quantitative NAD(P)H/flavoprotein autofluorescence imaging reveals metabolic mechanisms of pancreatic islet pyruvate response.* J Biol Chem, 2004. **279**(30): p. 31780-7.

104.   Huang, S., A.A. Heikal, and W.W. Webb, *Two-photon fluorescence spectroscopy and microscopy of NAD(P)H and flavoprotein.* Biophys J, 2002. **82**(5): p. 2811-25.

105.   Kunz, W.S. and W. Kunz, *Contribution of different enzymes to flavoprotein fluorescence of isolated rat liver mitochondria.* Biochim Biophys Acta, 1985. **841**(3): p. 237-46.

106.   Chance, B. and B. Thorell, *Localization and kinetics of reduced pyridine nucleotide in living cells by microfluorometry.* J Biol Chem, 1959. **234**: p. 3044-50.

107.   Quinn, K.P., et al., *Quantitative metabolic imaging using endogenous fluorescence to detect stem cell differentiation.* Sci Rep, 2013. **3**: p. 3432.

108.   Fernyhough, P., *Mitochondrial dysfunction in diabetic neuropathy: a series of unfortunate metabolic events.* Curr Diab Rep, 2015. **15**(11): p. 89.

109.   Parra-Bonilla, G., et al., *Critical role for lactate dehydrogenase A in aerobic glycolysis that sustains pulmonary microvascular endothelial cell proliferation.* Am J Physiol Lung Cell Mol Physiol, 2010. **299**(4): p. L513-22.

110.   Vazquez-Martin, A., et al., *The mitochondrial H(+)-ATP synthase and the lipogenic switch: new core components of metabolic reprogramming in induced pluripotent stem (iPS) cells.* Cell Cycle, 2013. **12**(2): p. 207-18.

111.   De Bock, K., et al., *Role of PFKFB3-driven glycolysis in vessel sprouting.* Cell, 2013. **154**(3): p. 651-63.

112.   Ferre, P. and F. Foufelle, *SREBP-1c transcription factor and lipid homeostasis: clinical perspective.* Horm Res, 2007. **68**(2): p. 72-82.

113.   Anderson, S.M., et al., *Key stages in mammary gland development. Secretory activation in the mammary gland: it's not just about milk protein synthesis!* Breast Cancer Res, 2007. **9**(1): p. 204.

114.   Menendez, J.A. and R. Lupu, *Fatty acid synthase and the lipogenic phenotype in cancer pathogenesis.* Nat Rev Cancer, 2007. **7**(10): p. 763-77.

115.   Georgakoudi, I. and K.P. Quinn, *Optical imaging using endogenous contrast to assess metabolic state.* Annu Rev Biomed Eng, 2012. **14**: p. 351-67.

116.   Melissa C. Skala, K.M.R., Annette Gendron-Fitzpatrick, Jens Eickhoff, Kevin W. Eliceiri, John G. White, and Nirmala Ramanujam, *In vivo multiphoton microscopy of NADH and FAD redox states, fluorescence lifetimes, and cellular morphology in precancerous epithelia.* PNAS, 2007. **104**(49): p. 19494-19499.

117.   Hou, J., et al., *Correlating two-photon excited fluorescence imaging of breast cancer cellular redox state with seahorse flux analysis of normalized cellular oxygen consumption.* J Biomed Opt, 2016. **21**(6): p. 60503.

118.   Zhang, Z., et al., *Plk1 inhibition enhances the efficacy of androgen signaling blockade in castration-resistant prostate cancer.* Cancer Res, 2014. **74**(22): p. 6635-47.

119.   Alfonso-Garcia, A., et al., *Biological imaging with coherent Raman scattering microscopy: a tutorial.* J Biomed Opt, 2014. **19**(7): p. 71407.

120.   hua Yue, J.M.C.-M., Lesley S. Chaboub, Sophie A. Lelievre and Ji-Xin Cheng, *Label-Free Analysis of Breast Tissue Polarity by Raman Imaging of Lipid Phase.* Biophysical Journal, 2012. **102**: p. 8.

121.   Paolo P. Provenzano, K.W.E., Long Yan, Aude Ada-Nguema, Matthew W. Conklin, David R. Inman, and Patricia J. Keely, *Nonlinear Optical Imaging of Cellular Processes in Breast Cancer.* Microscopy Microanalysis, 2008. **14**: p. 16.

122.   Bissell, C.M.G.M.J., *Extracellular matrix control of mammary gland morphogenesis and tumorigenesis: insights from imaging.* Histochem Cell Biol, 2008. **130**: p. 13.

123.   Li, J. and J.X. Cheng, *Direct visualization of de novo lipogenesis in single living cells.* Sci Rep, 2014. **4**: p. 6807.

124.   Alfonso-Garcia, A., et al., *D38-cholesterol as a Raman active probe for imaging intracellular cholesterol storage.* J Biomed Opt, 2016. **21**(6): p. 61003.

125.   Reiske, H.R., et al., *Analysis of FAK-associated signaling pathways in the regulation of cell cycle progression.* Febs Letters, 2000. **486**(3): p. 275-280.

126.   Lloyd, S.M., J. Arnold, and A. Sreekumar, *Metabolomic profiling of hormone-dependent cancers: a bird's eye view.* Trends Endocrinol Metab, 2015. **26**(9): p. 477-85.

127.   Gerard, C. and A. Goldbeter, *The balance between cell cycle arrest and cell proliferation: control by the extracellular matrix and by contact inhibition.* Interface Focus, 2014. **4**(3).

128. Valerie M. Weaver, S.L., Johnathon N. Lakins, Micah A. Chrenek, Jonathan C.R. Jones, Filippo Giancotti, Zena Werb, and Mina J. Bissell, *β4 integrin-dependent formation of polarized three-dimensional architecture confers resistance to apoptosis in normal and malignant mammary epithelium.* cancer cell, 2002. **2**(3): p. 11.

129. Clarkson, R.W.E., et al., *NF-kappa B inhibits apoptosis in murine mammary epithelia.* Journal of Biological Chemistry, 2000. **275**(17): p. 12737-12742.

130. Ghukasyan, V.V. and A.A. Heikal, *Natural biomarkers for cellular metabolism : biology, techniques, and applications*. 2015.

131. Sobolewska, A., T. Motyl, and M. Gajewska, *Role and regulation of autophagy in the development of acinar structures formed by bovine BME-UV1 mammary epithelial cells.* Eur J Cell Biol, 2011. **90**(10): p. 854-64.

132. Weigelt, B., F.C. Geyer, and J.S. Reis-Filho, *Histological types of breast cancer: how special are they?* Mol Oncol, 2010. **4**(3): p. 192-208.

133. Walsh, A., et al., *Optical imaging of metabolism in HER2 overexpressing breast cancer cells.* Biomed Opt Express, 2012. **3**(1): p. 75-85.

134. Walsh, A.J., et al., *Ex vivo optical metabolic measurements from cultured tissue reflect in vivo tissue status.* J Biomed Opt, 2012. **17**(11): p. 116015.

135. Claudia Nieva, M.M., Naiara Santana-Codina, Satish Rao, Dmitri Petrov, Angels Sierra, *The Lipid Phenotype of Breast Cancer Cells Characterized by Raman Microspectroscopy: Towards a Stratification of Malignancy.* PLOS ONE, 2012. **7**(10): p. 10.

136. Baenke, F., et al., *Hooked on fat: the role of lipid synthesis in cancer metabolism and tumour development.* Dis Model Mech, 2013. **6**(6): p. 1353-63.

137. Russell, T.D., et al., *Cytoplasmic lipid droplet accumulation in developing mammary epithelial cells: roles of adipophilin and lipid metabolism.* J Lipid Res, 2007. **48**(7): p. 1463-75.

138. Russell, T.D., et al., *Adipophilin regulates maturation of cytoplasmic lipid droplets and alveolae in differentiating mammary glands.* J Cell Sci, 2011. **124**(Pt 19): p. 3247-53.

139. Rudolph, M.C., et al., *Functional development of the mammary gland: use of expression profiling and trajectory clustering to reveal changes in gene expression during pregnancy, lactation, and involution.* J Mammary Gland Biol Neoplasia, 2003. **8**(3): p. 287-307.

140. Zhang, F. and G. Du, *Dysregulated lipid metabolism in cancer.* World J Biol Chem, 2012. **3**(8): p. 167-74.

141. Grevengoed, T.J., E.L. Klett, and R.A. Coleman, *Acyl-CoA metabolism and partitioning.* Annu Rev Nutr, 2014. **34**: p. 1-30.

142. Wilson, K.E., et al., *Multiparametric spectroscopic photoacoustic imaging of breast cancer development in a transgenic mouse model.* Theranostics, 2014. **4**(11): p. 1062-71.

143. Uray, I.P., et al., *Cancer-preventive rexinoid modulates neutral lipid contents of mammary epithelial cells through a peroxisome proliferator-activated receptor γ-dependent mechanism.* Mol Pharmacol, 2012. **81**(2): p. 228-38.

144. Park, J.H., et al., *Fatty Acid Oxidation-Driven Src Links Mitochondrial Energy Reprogramming and Oncogenic Properties in Triple-Negative Breast Cancer.* Cell Rep, 2016. **14**(9): p. 2154-65.

145. Camarda, R., et al., *Inhibition of fatty acid oxidation as a therapy for MYC-overexpressing triple-negative breast cancer.* Nat Med, 2016. **22**(4): p. 427-32.

146. Razandi, M., et al., *Tamoxifen regulates cell fate through mitochondrial estrogen receptor beta in breast cancer.* Oncogene, 2013. **32**(27): p. 3274-85.

147. Pedram, A., et al., *Membrane-localized estrogen receptor alpha is required for normal organ development and function.* Dev Cell, 2014. **29**(4): p. 482-90.

148. Mady, E.A., E.E. Ramadan, and A.A. Ossman, *Sex steroid hormones in serum and tissue of benign and malignant breast tumor patients.* Dis Markers, 2000. **16**(3-4): p. 151-7.

149.   Aguilera, K.Y., et al., *Collagen Signaling Enhances Tumor Progression after Anti-VEGF Therapy in a Murine Model of Pancreatic Ductal Adenocarcinoma.* Cancer Research, 2014. **74**(4): p. 1032-1044.

150.   Kenny, P.A., et al., *The morphologies of breast cancer cell lines in three-dimensional assays correlate with their profiles of gene expression.* Mol Oncol, 2007. **1**(1): p. 84-96.

151.   Brabrand, A., et al., *Alterations in collagen fibre patterns in breast cancer. A premise for tumour invasiveness?* Apmis, 2015. **123**(1): p. 1-8.

152.   Balaban, S., et al., *Obesity and cancer progression: is there a role of fatty acid metabolism?* Biomed Res Int, 2015. **2015**: p. 274585.

153.   Walther, T.C. and R.V. Farese, Jr., *Lipid droplets and cellular lipid metabolism.* Annu Rev Biochem, 2012. **81**: p. 687-714.

154.   Lupu, J.A.M.a.R., *Fatty acid synthase and the lipogenic phenotype in cancer pathogenesis.* nature reviews, 2007. **7**: p. 14.

155.   Shah, T., et al., *Noninvasive imaging identifies new roles for cyclooxygenase-2 in choline and lipid metabolism of human breast cancer cells.* NMR Biomed, 2012. **25**(5): p. 746-54.

156.   Barba, I., M.E. Cabanas, and C. Arus, *The relationship between nuclear magnetic resonance-visible lipids, lipid droplets, and cell proliferation in cultured C6 cells.* Cancer Res, 1999. **59**(8): p. 1861-8.

157.   Weinhouse, S., A. Allen, and R.H. Millington, *Metabolism of neoplastic tissue. V. Fatty acid oxidation in slices of transplanted tumors.* Cancer Res, 1953. **13**(4-5): p. 367-71.